Magnetic-Field-Enhanced Oxygen Evolution in Yttrium-Doped $CoFe_2O_4$ Langmuir-Blodgett Nanofilms

Viviana Beatriz Daboin Lujano[a], Paula G. Bercoff[b], Julieta S. Riva[a]**

[a]CONICET, Instituto de Investigaciones en Fisicoquímica de Córdoba (INFIQC). Universidad Nacional de Córdoba, Facultad de Ciencias Químicas, Ciudad Universitaria, X5000HUA Córdoba, Argentina.
[b]CONICET, Instituto de Física Enrique Gaviola (IFEG). Universidad Nacional de Córdoba, Facultad de Matemática, Astronomía, Física y Computación, Ciudad Universitaria, X5000HUA Córdoba, Argentina.

* paula.bercoff@unc.edu.ar * julieta.riva@unc.edu.ar

Abstract

Pure cobalt ferrite ($CoFe_2O_4$) and yttrium-doped cobalt ferrite ($CoY_{0.2}Fe_{1.8}O_4$) nanofilms were fabricated using nanoparticles synthesized via a self-combustion route and assembled through the Langmuir-Blodgett (LB) technique. These nanostructured films were employed as anodes to investigate the effects of Y^{3+} incorporation in the structure and the application of an external magnetic field on the oxygen evolution reaction (OER). Transmission electron microscopy and X-ray diffraction confirmed a reduction in particle and crystallite size upon Y doping, while X-ray photoelectron spectroscopy evidenced Y^{3+} incorporation and partial cation redistribution within the spinel lattice. Magnetic measurements indicated ferrimagnetic behavior for both materials, with Y substitution decreasing the saturation magnetization and increasing the coercivity. The LB nanofilms exhibited homogeneous coverage and pronounced in-plane magnetic anisotropy, and were used as anodes for the OER in alkaline media. Y^{3+} doping significantly improved the OER activity by reducing the overpotential and charge-transfer resistance, whereas the application of a magnetic field further amplified the catalytic response (particularly under in-plane orientation) through the combined effects of spin polarization and Lorentz-force-induced magnetohydrodynamic convection. Remarkably, the magneto-enhancement observed in pure $CoFe_2O_4$ nanofilms was comparable to that achieved through Y doping, underscoring the potential of magnetic-field-assisted catalysis as a sustainable strategy to minimize reliance on rare-earth elements while maintaining high OER efficiency. Both electrodes maintained stable activity over prolonged cycling, confirming their structural and electrochemical robustness. This study highlights the dual role of rare-earth doping and magnetic-field effects in tailoring the spin, structural, and electronic properties of spinel ferrite nanofilms for next-generation energy conversion applications.

Keywords: Cobalt ferrite; Yttrium doping; Langmuir-Blodgett films; Oxygen evolution reaction (OER); Electrocatalysis; Magnetic nanomaterials

Introduction

Recent years have seen a growing effort to replace fossil fuels with renewable energy sources, reflecting a key global priority. However, this transition is hampered by natural fluctuations in sources such as solar, wind, and tidal energy, and an efficient energy storage pathway is needed for situations where production levels do not match consumption. Electrocatalytic water splitting offers a promising pathway, producing green H_2 when fueled by renewable energy.[1] However, the process is limited by the slow kinetics and high overpotential of the oxygen evolution reaction (OER), and because it proceeds through a multistep proton-coupled electron transfer process. The efficient progression of the

OER critically depends on the design and development of effective electrocatalysts.

Catalysts based on noble metals such as Ru and Ir exhibit excellent OER performance in acidic media. However, their high cost, limited availability, and poor long-term chemical stability in alkaline media hinder their large-scale use. In contrast, oxides of inexpensive abundant metals have shown comparable reactivity in alkaline media, particularly oxide spinels containing Co, Ni, or Fe.[1,2] Among these, cobalt-based compounds have drawn significant attention, as materials such as cobalt oxides,[3] phosphates,[4] perovskites,[5] and (oxy)hydroxides[6] have demonstrated promising OER performance. In addition, spinel oxides, described by the general formula AB_2O_4, (where A and B denote metal ions), have recently gained significant attention for energy-related applications.[7] For example, Jagdeep S. Sagu et al. reported the excellent electrocatalytic activity of spinel $CoFe_2O_4$ prepared by low-cost aerosol-assisted chemical vapor deposition method towards the OER in an alkaline medium.[2] Several synthesis strategies have been developed for iron-cobalt oxides, including sonochemical, solvothermal, chemical co-precipitation, and electrochemical.[7-9] Among these synthesis methods, the self-combustion offers several advantages, including low cost, short reaction time, and high material yield.[10,11] It typically employs organic fuels such as urea,[12] glycine,[13] citric acid,[14] oxalyl dihydrazide,[15] or alanine[16] to enhance reaction efficiency. In this process, metal nitrate salts and fuel are mixed in stoichiometric proportions and heated to around 400 °C, initiating an exothermic reaction that leads to the formation of metal oxide nanoparticles (NPs).[11]

Tailoring the physicochemical properties of pure Co ferrite NPs for specific applications can be carried out by controlling size and shape, varying the synthesis method, and also by elemental substitution with different cations, which can further enhance their magnetic and electric characteristics.[17] In particular, doping $CoFe_2O_4$ spinel ferrites with rare-earth ions (Y^{3+}, Gd^{3+}, Ho^{3+}, Sm^{3+}, Nd^{3+}), which have a large ionic radii, distort the lattice, introducing structural disorder and strain. Also, these substitutions alter the magnetic coupling, consequently influencing the crystal structure (lattice parameter, crystallite size, grain morphology) and also the dielectric, magnetic, conductive, magnetostrictive and electrochemical properties of the material.[11] Furthermore, it has recently been reported that the presence of Yttrium in the ferrite structure can improve the electrochemical performance of the OER reaction.[18,19]

Another interesting way to improve OER kinetics comes from the application of external magnetic fields, since it is proposed that this could contribute to enhancing this reaction from different perspectives. On one hand, magnetic fields can enhance performance by affecting Lorentz-driven motion, thereby improving reagent and gas-bubble diffusion and enhancing mass transport.[20,21] On the other hand, performance improvements have also been reported under high-frequency alternating magnetic fields applied to magnetic nanoparticle-modified electrodes, by increasing local temperature in a hyperthermia-like process.[22] In addition, the spin polarization at the catalyst surface can promote parallel spin alignment of oxygen atoms, enhancing the reaction efficiency, since the formation of the O-O bond involves the cleavage of two water or OH^- molecules, which must proceed through spin conservation to produce molecular oxygen in its paramagnetic triplet state. The change in spin multiplicity between reactants and products contributes to the high overpotential and slow kinetics of OER. While H_2O and OH^- are singlets, O_2 has a triplet ground state, making spin regulation crucial to accelerate the reaction. In particular, magnetic fields applied to ferromagnetic catalysts such as $CoFe_2O_4$ enhance OER activity by promoting spin polarization and facilitating O-O triplet formation. [23,24]

In several applications, nanomaterials are typically used in their powdered form; however, assembling them into 2D films on solid surfaces could significantly expand their range of

applications. Most deposits onto conductive substrates are commonly prepared by dip-coating.[3,22] Nevertheless, this method often fails to ensure film homogeneity due to the *coffee-ring effect*, which can alter the distribution of nanoparticles drop-cast onto the electrode surface.[25] Among the techniques reported for the 2D assembly of NPs, the Langmuir-Blodgett (LB) has proved to be the most versatile method for fabricating NPs layers owing to the precise control it offers over film thickness and uniformity.[26,27] So far, several studies have successfully demonstrated the assembly of magnetic NPs using the LB technique. [28,29]

In this work, $CoFe_2O_4$ (CFO) and Y-doped $CoFe_{1.8}Y_{0.2}O_4$ (CFYO) nanoparticles were synthesized via a self-combustion route and subsequently coated with stearic acid to render them hydrophobic. Using the LB technique, these NPs were self-assembled onto conductive ITO substrates to form homogeneous nanostructured anodes for the oxygen evolution reaction (OER). We demonstrate that both Y^{3+} doping and the application of an external magnetic field significantly enhance the electrocatalytic performance of these magnetic anodes under alkaline conditions. The results reveal that the magnetic field exerts a pronounced influence on the OER activity, with the observed magneto-enhancement intimately linked to the intrinsic magnetic properties of the catalysts. Notably, this magnetic-field-induced improvement in catalytic performance offers a promising strategy to enhance the activity of simple, low-cost ferrite materials, potentially reducing or eliminating the need for rare-earth doping in next-generation OER electrodes.

Materials and methods

Synthesis of CFO and CFYO nanoparticles

Cobalt ferrite ($CoFe_2O_4$) and yttrium-doped cobalt ferrite ($CoFe_{1.8}Y_{0.2}O_4$) nanoparticles were synthesized by a self-combustion method, as previously reported.[10] Throughout the manuscript, these materials are referred to as CFO and CFYO, respectively.

Briefly, to synthesize CFO, stoichiometric amounts of iron (III) nitrate and cobalt (II) oxalate were dissolved in distilled water to obtain a final metal ion concentration of 1 M. Then, 50 mL of a 3 M citric acid solution was added to 50 mL of the metal solution and the mixture was heated at 40 °C under constant stirring for approximately 30 minutes. A viscous gel formed upon slow evaporation at temperatures below 200 °C, eventually igniting in a self-sustained combustion reaction. The resulting powder was collected and calcined at 800 °C for 2 hours. CFYO nanoparticles were synthesized using the same procedure, with the addition of yttrium nitrate to the precursor solution.

The as-prepared nanoparticles were further modified with stearic acid (SA) according to previously reported procedures.[11,30] Briefly, 0.15 g of CFO or CFYO were dispersed in a mixed solution of absolute ethanol (25 mL) and stearic acid (0.075 g). The suspensions were sonicated at 80 °C for 1 hour and washed five times with ethanol to remove excess SA. Finally, the powders were dried at 60 °C for 24 hours.

Preparation of ITO/ CFO and ITO/ CFYO nanofilms

To deposit the SA-modified CFO and CFYO nanoparticles onto conductive substrates, the Langmuir-Blodgett (LB) technique was employed, as previously reported for similar systems.[11,19] Nanoparticle suspensions with a concentration of 5 mg/mL were prepared, using a chloroform-methanol mixture as solvent. A volume of 300 µL of each suspension was carefully spread onto the air/water interface (Milli-Q, 18.2 MΩ·cm, Millipore) of a Langmuir trough using a microsyringe.

Surface pressure-area isotherms of the resulting ITO/CFO and ITO/CFYO nanofilms were recorded using a Wilhelmy plate coupled to a KSV Mini-Trough system (36.4 cm × 7.5 cm, KSV Model 2000). After allowing ~20 min for solvent evaporation, the nanoparticles were

compressed at a rate of 10 mm/min. The resulting films were transferred onto ITO-coated glass substrates at a surface pressure of 40 mN/m and a dipping speed of 3 mm/min, by vertically immersing and withdrawing the substrate through the subphase (see Scheme 1).

To ensure homogeneous coverage, the deposition process was repeated twice for each sample.

Prior to deposition, the ITO substrates were cleaned sequentially with acetone, ethanol, and Milli-Q water, followed by hexane treatment.

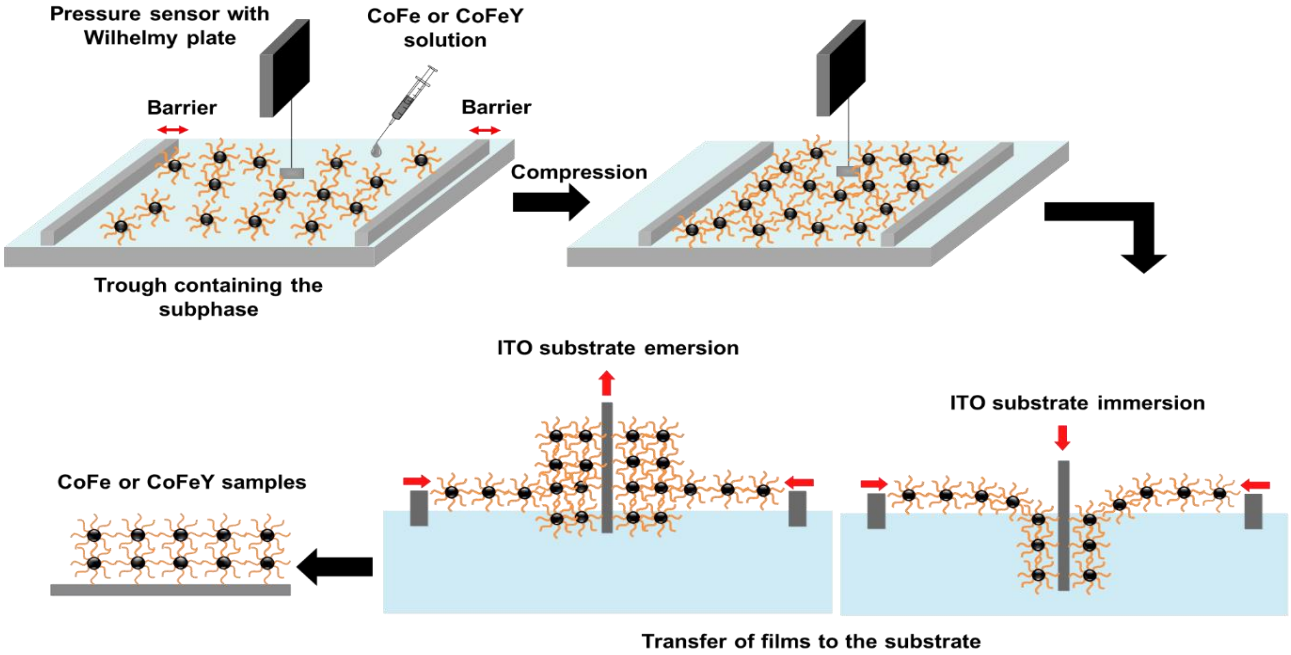

Scheme 1. Schematic illustration of the preparation of ITO/CFO and ITO/CFYO nanofilms by the Langmuir-Blodgett method, showing the transfer of nanoparticles onto the ITO substrate.

Experimental Techniques

CFO and CFYO nanoparticles and nanofilms were characterized using various techniques. The crystalline structure was analyzed by X-ray powder diffraction (XRD) using a PANalytical X'Pert Pro diffractometer operating in Bragg-Brentano geometry with Cu Kα radiation (λ = 1.5418 Å), at 40 kV and 40 mA.

The morphology of the NPs and the thickness of the films were examined using a Sigma Zeiss Field Emission Scanning Electron Microscope (FE-SEM) and an Agilent Technologies 5500 Atomic Force Microscope (AFM). AFM measurements were carried out in tapping mode under ambient conditions using rotated monolithic silicon probes coated with an aluminum reflex film (Budget Sensors TAP150-Al-G; nominal spring constant: 5 $N \cdot m^{-1}$; resonance frequency: 150 kHz; nominal tip radius: <10 nm). Transmission electron microscopy (TEM) was performed on a Hitachi 7800 microscope operated at an accelerating voltage of 100 kV.

X-ray Photoelectron Spectroscopy (XPS) spectra were acquired with a Thermo Fisher Scientific K-Alpha spectrometer equipped with a monochromatic Al Kα X-ray source (LAMARX-FAMAF-UNC). Survey and high-resolution spectra were obtained by averaging multiple scans, using an energy step size of 0.5 eV for survey scans and 0.05 eV for high-resolution spectra. The total acquisition time was 7 minutes.

Magnetic characterization was carried out using a Cryogenic Ltd. vibrating sample magnetometer (VSM) at 300 K with applied magnetic fields up to ±5 T. For these measurements, the nanoparticles were pressed into thin pellet disks. The nanofilms were measured under an external magnetic field applied both parallel (in-plane, IP) and perpendicular (out-of-plane, OoP) to the substrate surface. A bare glass substrate was also measured under the same conditions, and its magnetic contribution was subtracted from the nanofilms data.

Electrochemical measurements

The electrochemical performance of the ITO/CFO and ITO/CFYO nanofilms was evaluated using a conventional three-electrode system connected to a CHI 760C electrochemical workstation. The ITO-coated glass substrates bearing the CFO and CFYO nanofilms were used directly as working electrodes. A platinum foil served as the counter electrode, and an Ag/AgCl (in 1 M KOH) electrode was used as the reference.

All measurements were carried out in a 0.1 M KOH (pH = 13.0) aqueous solution. The recorded potentials were converted to the reversible hydrogen electrode (RHE) scale using the Nernst equation: $E_{RHE} = E_{Ag/AgCl} + 0.059 \times pH + 0.197$ V. The overpotential (η) was calculated as: η (V) = E_{RHE} - 1.23 V. Polarization current densities were normalized to the geometric surface area of the electrode.

Linear sweep voltammetry (LSV) was conducted at a scan rate of 25 mV·s^{-1}. Tafel slopes were extracted from the LSV curves by fitting to the Tafel equation: $\eta = a + b \cdot \log j$, where j is the current density, b is the Tafel slope, and a is a constant. Electrochemical impedance spectroscopy (EIS) was performed at 1.7 V vs RHE in the frequency range from 0.01 Hz to 1000 Hz, using an amplitude of 5 mV. The resulting data were fitted with equivalent circuit models using ZPLOT/ZVIEW software (Scribner Associates, Inc.). Stability and durability tests were conducted by cyclic voltammetry (CV) for 400 consecutive cycles.

To evaluate the effect of an external magnetic field on the electrochemical response, measurements were performed under a constant magnetic field applied in both in-plane (IP) and out-of-plane (OoP) configurations with respect to the nanofilm surface. Different permanent magnets were placed externally by the electrochemical cell to generate magnetic fields with different intensities (45 mT and 130 mT). They were positioned parallel to the film plane (IP configuration), and subsequently in a perpendicular orientation (OoP configuration). The distance between the magnet and the working electrode was kept constant at approximately 1 cm in all measurements. The magnetic field intensity was continuously monitored using a handheld digital teslameter. A schematic representation of the experimental setup is shown in Scheme 2.

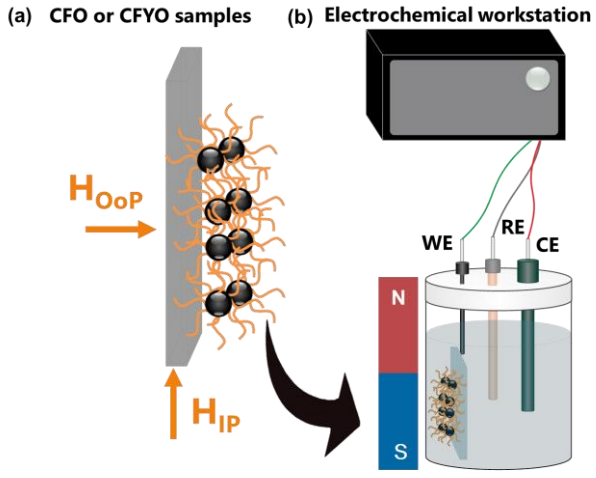

Scheme 2. (a) Schematic representation of the obtained nanofilms, indicating the in-plane (IP) and out-of-plane (OoP) field orientations used for magnetic and electrochemical measurements. (b) Experimental setup for electrochemical characterization.

Results and Discussion

Characterization of the NPs

TEM images (Figure 1(a), (c)) show that CFO and CFYO NPs exhibit a rounded morphology. The mean diameters, determined from the corresponding histograms (Figure 1(b), (d)), were (84 ± 2) nm for CFO and (46 ± 2) nm for CFYO. The absence of extensive agglomeration indicates that the synthesis and subsequent surface modification steps were effective in preventing particle aggregation.

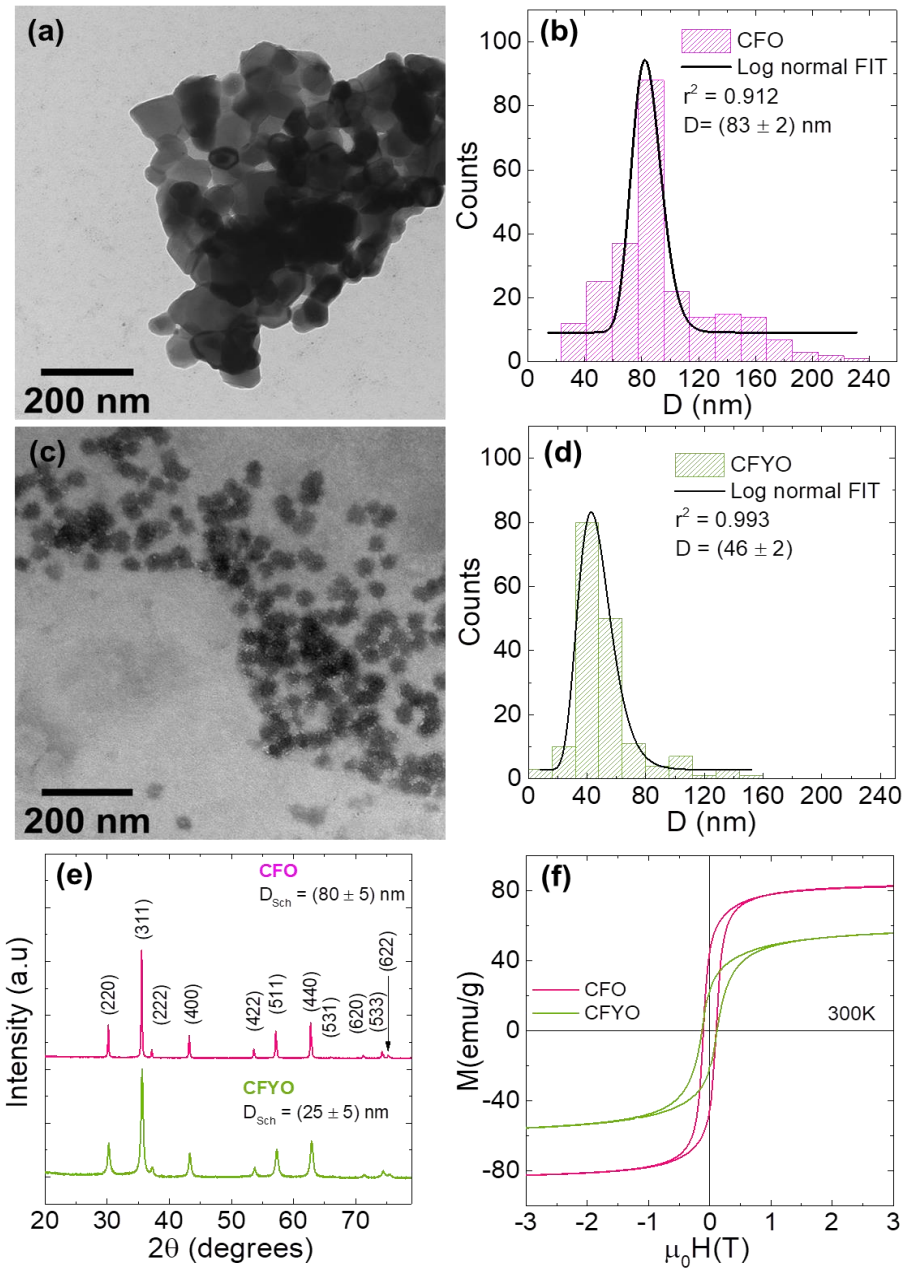

Figure 1. (a) TEM image and (b) particle size distribution histogram of CFO; (c) TEM image and (d) particle size distribution of CFYO. (e) XRD patterns and (f) magnetic hysteresis loops measured at 300 K for CFO (pink line) and CFYO (green line). The maximum applied magnetic field was ±5 T; however, only the ±3 T range is shown for clarity.

The crystalline structure was analyzed by XRD (Figure 1(e)). In both samples, the diffraction peaks match well with the standard spinel cobalt ferrite phase (JCPDS-PDF 22-1086), confirming the successful formation of the $CoFe_2O_4$ spinel structure. No additional peaks from secondary phases were detected. The lattice parameters, calculated from the XRD patterns, were 8.3718(4) Å for CoFe and 8.3574(6) Å for CoFeY, indicating a slight lattice contraction upon Y^{3+} incorporation.

The average crystallite sizes, calculated using the Scherrer equation, were (80 ± 5) nm for CFO and (25 ± 5) nm for CFYO. The smaller crystallite sizes obtained from XRD compared to the particle diameters observed by TEM suggest that the nanoparticles are polycrystalline, consisting of several coherently diffracting domains within a single particle. These results confirm that yttrium incorporation into the lattice reduces both the grain size and the particle size, as also observed by TEM.

Magnetic hysteresis loops recorded at 300 K (Figure 1(f)) exhibit the typical ferrimagnetic behavior of cobalt ferrite. The saturation magnetization (M_S) was (84 ± 3) emu/g for CoFe and (58 ± 3) emu/g for CoFeY, while the coercive field (H_C) values were (105 ± 1) mT and (124 ± 1) mT, respectively. The lower M_S in the Y-doped sample arises from the combined effect of Y^{3+} incorporation into the spinel lattice and the reduction in nanoparticle size. The replacement of magnetic Fe^{3+} ions by non-magnetic Y^{3+} ions weakens the superexchange interactions within the spinel lattice, thereby reducing the net magnetization.

High-resolution XPS spectra of: (b) Fe 2p, (c) Co 2p, (d) Y 3d (only for sample CFYO), (e) C 1s, and (f) O 1s. All peaks have been deconvoluted. The spectra corresponding to CFO and CFYO are distinguished by the color-coded legend in the figure.

In addition, the smaller nanoparticle size in CFYO have a larger surface-to-volume ratio, increasing the contribution of surface spins that are more prone to canting or magnetic disorder, which further decreases the net magnetization at room temperature.[11] According to the well-established Stoner-Wohlfarth model, the observed increase in H_C from CFO to CFYO is a consequence of the particle size reduction and the decrease in M_S, since $H_C \propto 1/M_S$.[11, 17]

The XPS survey spectra of stearic-acid-coated CFO and CFYO NPs are shown in Figure 2(a). Peaks corresponding to Fe, Co, O, and C are visible in both samples, while an additional Y signal appears in the CFYO spectrum. The binding energies (BE) were calibrated using the C 1s peak at 284.8 eV as an internal reference. No other elements were detected, confirming the high purity of the samples. High-resolution spectra were measured for Fe, Co, Y, C and O and the parameters obtained from their analysis are listed in Table S1, in the Supplementary Information.

The high-resolution Fe 2p spectra of the NPs (Figure 2(b)) display two main peaks centered at ~710 eV and ~724 eV, corresponding to Fe $2p_{3/2}$ and Fe $2p_{1/2}$, respectively. The Fe $2p_{3/2}$ band is deconvoluted into two components at 710.24 eV and 712.72 eV, attributed to Fe^{3+} ions located at octahedral and tetrahedral sites.[30,31] Quantitative analysis of the peak areas indicates Fe^{3+} site occupancies of 68.20% (octahedral) and 31.80% (tetrahedral) for CFO, and 57.24% (octahedral) and 42.76% (tetrahedral) for CFYO. Similarly, the Co 2p spectra (Figure 2(c)) exhibit two main peaks at 779.9 eV and 795.4 eV, corresponding to the Co $2p_{3/2}$ and Co $2p_{1/2}$ spin-orbit components, respectively, along with satellite peaks at ~786 eV and ~802 eV. The Co $2p_{3/2}$ peak is deconvoluted into two components at 779.9 eV and 795.0 eV, associated with Co^{2+} ions at octahedral and tetrahedral sites of the spinel lattice.[6,7] The relative Co^{2+} site occupancies are 58.70% (octahedral) and 41.30% (tetrahedral) for CFO, and 53.08% (octahedral) and 46.92% (tetrahedral) for CFYO. The slightly higher BE values in CFYO are consistent with the presence of Y^{3+} cations.

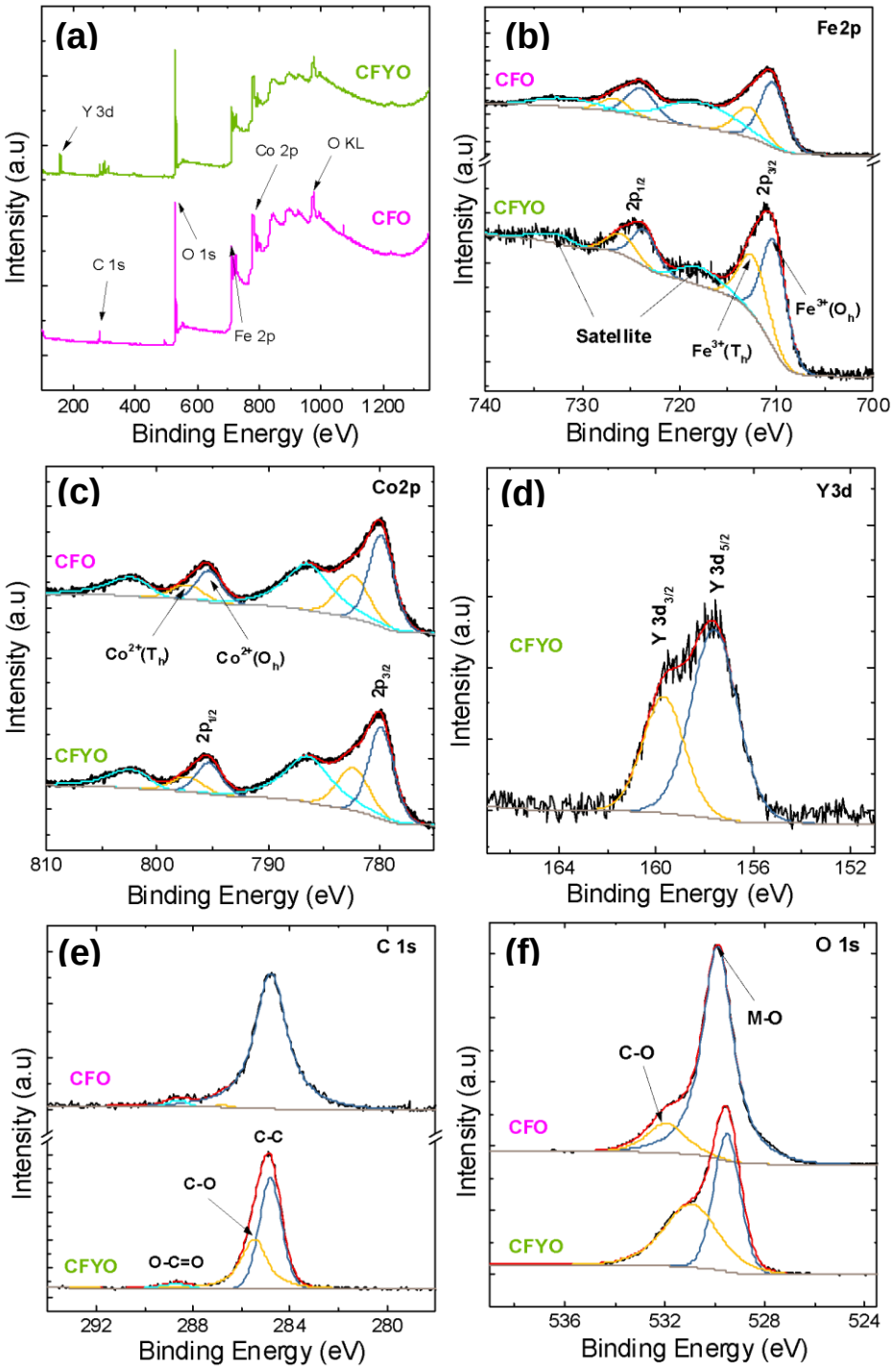

Figure 2. (a) XPS survey spectra of CFO and CFYO nanoparticles.

The reduction in Co^{2+} and Fe^{3+} occupancy at octahedral sites in CFYO can be explained by Y^{3+} incorporation. Y^{3+} preferentially substitutes Fe^{3+} in octahedral coordination, inducing lattice strain.[1] To compensate, a fraction of Co^{2+} migrates from octahedral to tetrahedral sites, modifying the cation distribution and slightly reducing the unit cell size. This redistribution is consistent with previous reports on rare-earth-doped spinels,

where a structural accommodation mechanism rather than a vacancy-driven process occurs.[32,33]

The Y 3d spectrum (Figure 2(d)) of CFYO exhibits two components at ~158 eV and ~160 eV, assigned to Y $3d_{5/2}$ (Y-O bonds) and Y $3d_{3/2}$ (Y^{3+}), respectively.[34]

The C 1s spectra (Figure 2(e)) show a main peak at 284.8 eV, attributed to aliphatic C-C and C-H bonds, likely originating from the decomposition of the citrate fuel during synthesis, and confirming the presence of the organic coating agent on the nanoparticles. The O 1s spectra (Figure 2(f)) have a main peak at 529.5 eV, which can be deconvoluted into three components. The peaks at 529.5 eV and 531.56 eV are assigned to M-O-M (M = metal) bonds and C-O species, respectively, the latter likely originating from stearic acid groups, residual citrate, or adsorbed CO_2 on the particle surface.[11,17]

Pressure-area isotherms of CFO and CFYO nanofilms

Figure 3(a) shows the surface pressure-area (π-A) isotherms for CFO (pink line) and CFYO (green line) films, recorded to determine the optimal conditions for nanoparticle transfer onto the ITO substrate and nanofilm formation. Before barrier compression, CFO and CFYO NPs are in the gaseous phase, fully dispersed at the air-water interface without significant interactions, as illustrated schematically in Figure 3(b). This scheme depicts how the available surface area per NP decreases progressively as the barriers compress the nanoparticles, promoting the transition from a loosely packed arrangement to a closely packed structure.

The isotherm corresponding to CFYO exhibits well-defined gaseous, liquid, and solid phases, as well as a clear collapse point. During compression, the surface pressure remains nearly constant up to ~110 cm^2, which is characteristic of the gaseous phase in Langmuir films. Beyond this point, the pressure increases progressively, indicating the onset of the liquid phase and the formation of NP domains. At ~85 cm^2, the slope becomes steeper, marking the transition to the solid phase, where tighter packing of the NPs leads to larger ordered domains. Further compression below ~75 cm^2 induces molecular disorder and film collapse.

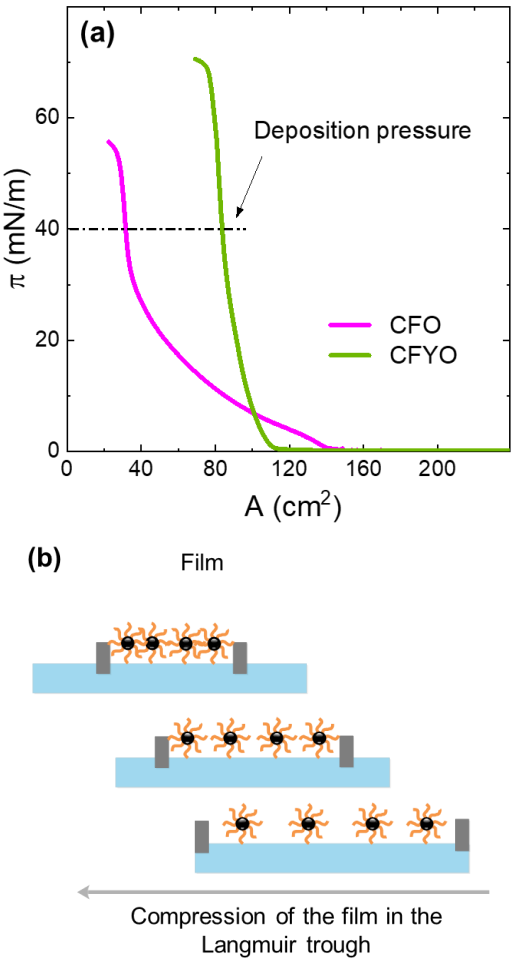

Figure 3. (a) Surface pressure-area isotherms of CFO (pink line) and CFYO (green line) nanoparticles spread on a water subphase. The dashed horizontal line marks the surface pressure of 40 $mN \cdot m^{-1}$ used for Langmuir-Blodgett transfer, chosen to ensure film stability and to avoid collapse of the nanoparticle layer. (b) Schematic representation of the compression process in the Langmuir trough during nanofilm formation. The scheme is not intended to represent an ideal close-packed monolayer, but rather a generic interfacial film formed upon compression, which may present lateral and vertical heterogeneities.

In contrast, the CoFe isotherm shows a gaseous phase up to ~140 cm^2, but the liquid phase is less distinctly defined. Upon continuous compression, the surface pressure increases gradually, reaching a steeper slope at ~40 cm^2, reflecting solid-phase formation and compact NP packing. The more gradual pressure increase observed for CFO suggests reduced mobility of nanoparticle aggregates at the air-water interface, indicative of aggregation effects during compression.

Based on these π-A isotherms, a surface pressure of 40 mN/m was selected as the optimal deposition condition, since at this value the nanoparticles are predominantly in the solid phase. The efficiency of the Langmuir-Blodgett deposition was evaluated through the transfer ratio, defined as the ratio between the decrease in monolayer area at the air-water interface during compression and the area of the solid substrate onto which the film is transferred. Under these conditions, multiple nanoparticle layers were successfully transferred onto hydrophobic ITO substrates, achieving maximum transfer ratios of 1.2 ± 0.2 (immersion) and 0.3 ± 0.1 (emersion) for CFO, and 1.4 ± 0.2 (immersion) and 0.5 ± 0.2 (emersion) for CFYO, indicating an efficient transfer of compact nanoparticle films. These observations are consistent with aggregation effects later evidenced by SEM and AFM analyses, indicating that nanoparticle aggregation plays an important role in determining monolayer compressibility and the resulting film organization.

Characterization of ITO/CFO and ITO/CFYO nanofilms

Figure 4 presents the morphological and magnetic characterization of the nanofilms obtained by transferring nanoparticles onto ITO substrates via the Langmuir-Blodgett technique. SEM images of ITO/CFO (Figure 4(a)) and ITO/CFYO (Figure 4(b)) nanofilms reveal densely packed NP assemblies, indicative of an efficient transfer at the air-water interface. These images are representative of the entire substrate surface, evidencing the formation of continuous nanoparticle layers. The films display some NP clusters distributed across the surface, as evidenced by the insets in Figure 4(a) and Figure 4(b). These clustered arrangements arise during the Langmuir-Blodgett film formation process and should be distinguished from NP aggregation during synthesis, which is effectively prevented by the surface modification, as discussed above.

AFM analysis provides complementary topographical information for ITO/CFO (Figure 4(c)) and ITO/CFYO (Figure 4(d)) films. In both cases, bright zones correspond to NP agglomerates, corroborating the observations from SEM. Quantitative roughness analysis yields root mean square (RMS) roughness values of approximately 40 nm for ITO/CFO and 34 nm for ITO/CFYO films, reflecting a moderately rough surface originating from the multilayered NP assemblies formed during Langmuir-Blodgett deposition process. Cross-sectional profiles extracted from the AFM images (Figure S1 of the Supplementary Information) confirm that the nanofilms are composed of multiple NP layers, with estimated thicknesses of approximately 160 nm for ITO/CFO and 140 nm for ITO/CFYO.[11] AFM images of the film boundaries in 3D view, presented in Figure S1 of the Supplementary Information, further illustrate the transition between the substrate and the transferred nanofilm. Considering the mean particle sizes of both ferrites, it is concluded that a bilayer was obtained with CFO NPs, while the smaller CFYO NPs produced a trilayer nanofilm.

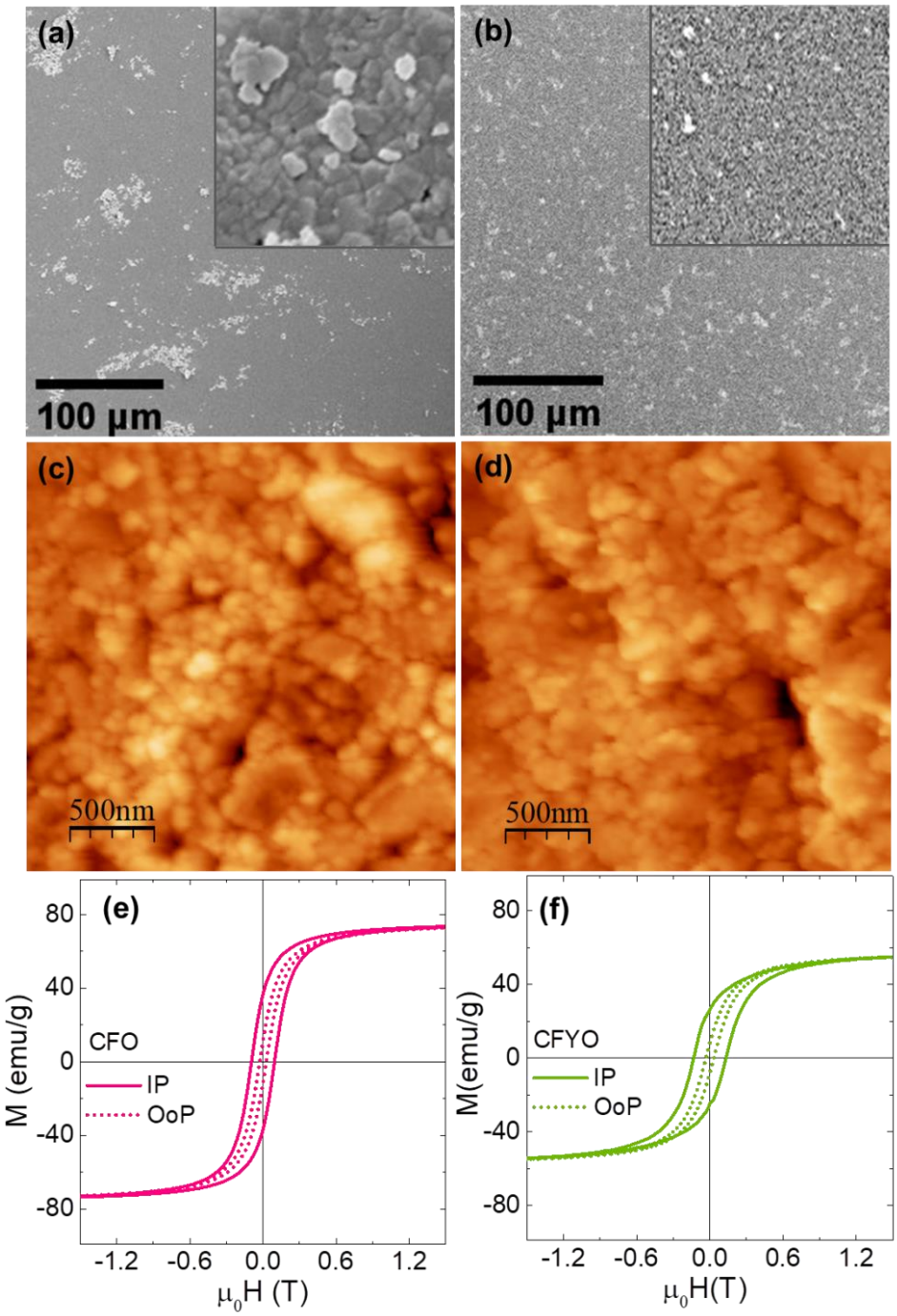

Figure 4. SEM image of (a) ITO/CFO and (b) ITO/CFYO nanofilms. The insets display higher magnifications, being the width of each image corresponding to 1 µm. AFM image of (c) ITO/ CFO and (d) ITO/CFYO. Magnetization curves under IP and OoP field orientations for (e) CFO and (f) CFYO.

The hysteresis loops for ITO/CFO and ITO/CFYO nanofilms, measured at room temperature with the magnetic field applied parallel (in-plane, IP) and perpendicular (out of plane, OoP) to the substrate, are shown in Figures 4(e) and 4(f), respectively. The maximum applied field was ±5 T in all cases, although only a reduced field range is displayed for clarity. The

paramagnetic contribution from the ITO substrates was subtracted from the raw data. In our previous works, we presented a comprehensive magnetic characterization of these films, including a detailed analysis of the temperature dependence of the magnetization processes in both films and nanoparticles.[11,17]

In both nanofilms, saturation magnetization M_S is essentially identical for IP and OoP orientations; however, the IP configuration exhibits higher magnetization values at low fields, indicating an easy magnetization plane parallel to the film's surface. This is consistent with the behavior expected for two-dimensional nanostructures with strong shape anisotropy.[11,17,35] Coercivity H_C is also higher for the IP orientation, further supporting the presence of in-plane magnetic anisotropy. The characteristic magnetic parameters extracted from the hysteresis loops are summarized in Table S2 of the Supplementary Information.

Although the nanofilms are composed of multilayers of NPs, giving rise to a locally quasi-3D magnetic structure similar to that of powder samples, their collective magnetic response is strongly governed by the macroscopic planar geometry of the assembly. As a result, the magnetic parameters (M_S, M_R, and H_C) reflect the interplay between bulk-like interparticle interactions within aggregates and the shape anisotropy imposed by the thin-film architecture, which favors an in-plane easy magnetization direction.

Oxygen evolution reaction performances of the nanofilms

The performance of ITO/CFO and ITO/CFYO nanofilms as anodes for the oxygen evolution reaction (OER) was evaluated by linear sweep voltammetry (LSV) in 0.1 M KOH using a standard three-electrode configuration. Figure 5(a) displays the LSV curves recorded between 1.3 and 2.3 V *vs*. RHE at a sweep rate of 25 $mV \cdot s^{-1}$.

For the same applied potential, the ITO/CFYO electrode exhibits higher OER current densities than ITO/CFO, indicating enhanced catalytic activity upon Y^{3+} incorporation. For instance, at an applied potential of 2.0 V, the current density is enhanced by 37% with ITO/CFO and by 300% with ITO/CFYO, relative to the bare ITO electrode.

The electrochemically active surface area (ECSA) and the corresponding roughness factor (*Rf*) are typically key parameters governing the enhanced catalytic activity observed in nanostructured catalysts.[22] In NP films, the ECSA determined from the double-layer capacitance (Cdl) represents an effective electrochemical surface area that accounts for porosity, possible NP aggregation, and electrolyte accessibility, rather than a purely geometric surface area. To elucidate the performance differences between ITO/CFO and ITO/CFYO anodes, the corresponding ECSA and *Rf* values were estimated from the electrochemical double-layer capacitance (Cdl), determined by cyclic voltammetry within the double-layer region at various scan rates (see Figure S2 in the Supplementary Information). Figure S3 shows the LSVs normalized to the ECSA. As observed, the trend remains the same as when the current is normalized only by the geometric area: the ITO/CoFeY anode exhibits the highest activity, followed by ITO/CoFe and, finally, the uncoated ITO. These results confirm that the superior catalytic performance arises from the intrinsic properties of the materials.

The corresponding Tafel plots derived from the LSV curves are shown in Figure 5(b) and Figure S4 and Figure S5 . A noticeable decrease in the Tafel slope is observed upon Y^{3+} incorporation, from 167 mV/dec for ITO/CFO to 119 mV/dec for ITO/CFYO. Since the Tafel slope is directly related to charge transfer kinetics, this reduction indicates that Y^{3+} doping facilitates electron transfer during the OER process. This improvement can be attributed to structural and electronic modifications in the spinel lattice, including the reduction in grain and particle sizes observed upon Y^{3+} incorporation, which increases the electrochemically active surface area and the

density of accessible catalytic sites. Similar beneficial effects have been reported in other oxide systems, where yttrium doping reduced particle size, altered cation distribution, and enhanced charge transport, ultimately improving surface reaction kinetics in photocatalytic and electrochemical processes.[36] Comparable improvements have also been observed in ZnO-based systems, where a similar doping mechanism leads to enhanced charge transport and improved catalytic performance.[37] The Tafel slopes obtained here (119 mV/dec for ITO/CFYO and 167 mV/dec for ITO/CFO) are within the range typically reported for cobalt ferrite-based OER electrocatalysts,[8,38] providing a useful baseline to assess the improvements induced under external magnetic fields, as discussed below (Figure 6).

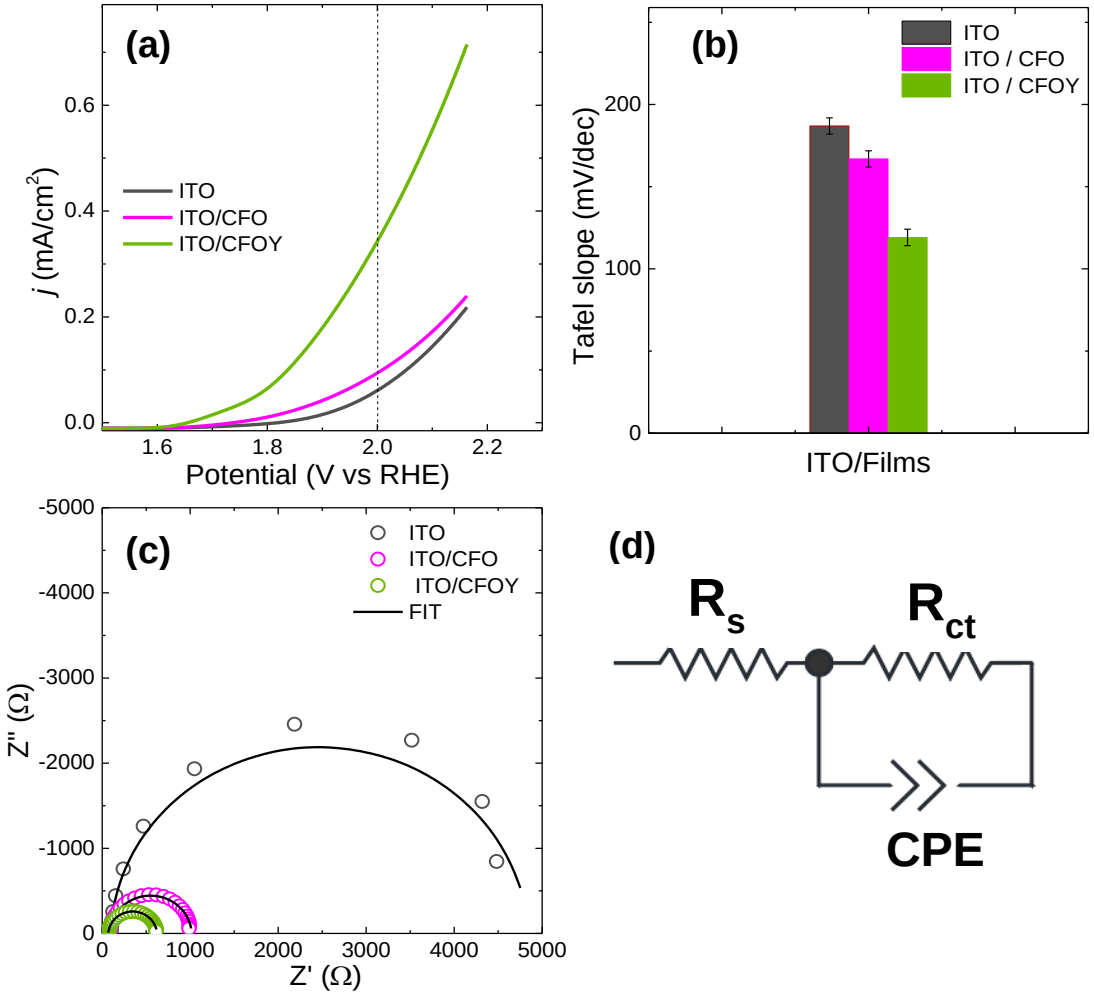

Figure 5. (a) LSV curves, (b) Tafel slopes, (c) Nyquist plots, and (d) equivalent circuits used to fit the EIS data for ITO, ITO/CFO, and ITO/CFYO electrodes. The dashed vertical line in (a) indicates the potential value at which the electrodes are compared (see text).

Electrochemical impedance spectroscopy (EIS) was performed at 1.7 V vs RHE to further investigate the interfacial charge transfer behavior (Figure 5(c)). Open dots represent the experimental data, while solid lines correspond to the best fitting results.

The Nyquist plots of ITO/CFO and ITO/CFYO electrodes display two distinct regions: a high-frequency intercept on the real axis corresponding to the solution resistance (*R*s) and a semicircular arc in the mid-to-low frequency range, associated with the charge transfer resistance (*R*ct) at the electrode/electrolyte interface. In this representation, the diameter (or radius) of the semicircle directly reflects the magnitude of *R*ct. Notably, the ITO/CFYO electrode exhibits a smaller semicircle diameter compared to ITO/CFO, indicating a lower *R*ct and, consequently, faster electron transfer kinetics during the OER. The pure ITO electrode shows the largest *R*ct, reflecting its negligible electrocatalytic activity.

The EIS data were fitted using the Randles equivalent circuit shown in Figure 5(d), where *R*s is the solution resistance, CPE is a constant phase element, and *R*ct is the charge transfer resistance. This circuit is consistent with the presence of a homogeneous film at the anode/electrolyte interface. The good agreement between the experimental data and the fitted model indicates that both ITO/CFO and ITO/CFYO nanofilms are composed of homogeneously distributed NP assemblies. The fitting parameters obtained from the model are summarized in Table S3 of the Supplementary Information, where the resistance trend *R*ct(ITO) ≫ *R*ct(ITO/CFO) > *R*ct(ITO/CFYO) is clearly observed, in agreement with the LSV and Tafel slope results. This behavior aligns with prior observations where conductive supports or compositional tuning significantly lower *R*ct, and with studies on cobalt-iron spinels showing drastic *R*ct reductions (from ~2000 Ω to ~10 Ω) upon increasing cobalt content.[8,39] These findings support that Y^{3+} doping enhances electrical conductivity and interfacial charge transfer in cobalt ferrite nanofilms, contributing to their improved OER performance.

Although the reduction in NP size upon Y^{3+} incorporation contributes to improved electrochemical performance, the significantly lower *R*ct and Tafel slope observed for CFYO indicate that compositional effects related to cation redistribution and electronic structure modification also play a key role.

Oxygen evolution reaction in the presence of a magnetic field

The influence of externally applied magnetic fields of varying intensities on the OER performance of ITO/CFO and ITO/CFYO nanofilms was investigated by LSV measurements under in-plane (IP) and out-of-plane (OoP) field configurations. These baseline values provide a useful reference to assess the improvements induced under external magnetic fields, as discussed below (Figure 6).

Figures 6(a) and 6(b) display the corresponding LSV curves for ITO/CFO and ITO/CFYO, respectively, recorded in 0.1 M KOH at a scan rate of 25 mV s^{-1}. Solid lines denote the IP field configuration, whereas dashed lines represent the OoP configuration.

In both nanofilms, the application of a magnetic field leads to an increase in current density relative to the zero-field condition, demonstrating a magnetically induced enhancement of the OER activity. The current density increases progressively with increasing field strength, indicating a distinct field-dependent catalytic response. This enhancement is more pronounced in the IP configuration for the ITO/CFO electrode, despite its overall current densities remaining lower than those of ITO/CFYO. At an applied potential of 2.0 V, the current density of the ITO/CoFe anode under a 130 mT magnetic field applied in the IP direction is enhanced by 287%, while the corresponding enhancement for the ITO/CFYO anode under the same conditions is 55%. These results demonstrate that, although the incorporation of rare-earth elements leads to intrinsically more efficient anodes, the application

of external stimuli such as magnetic fields can substantially improve the electrocatalytic performance of low-cost anode materials, particularly those exhibiting strong magnetic responsiveness.

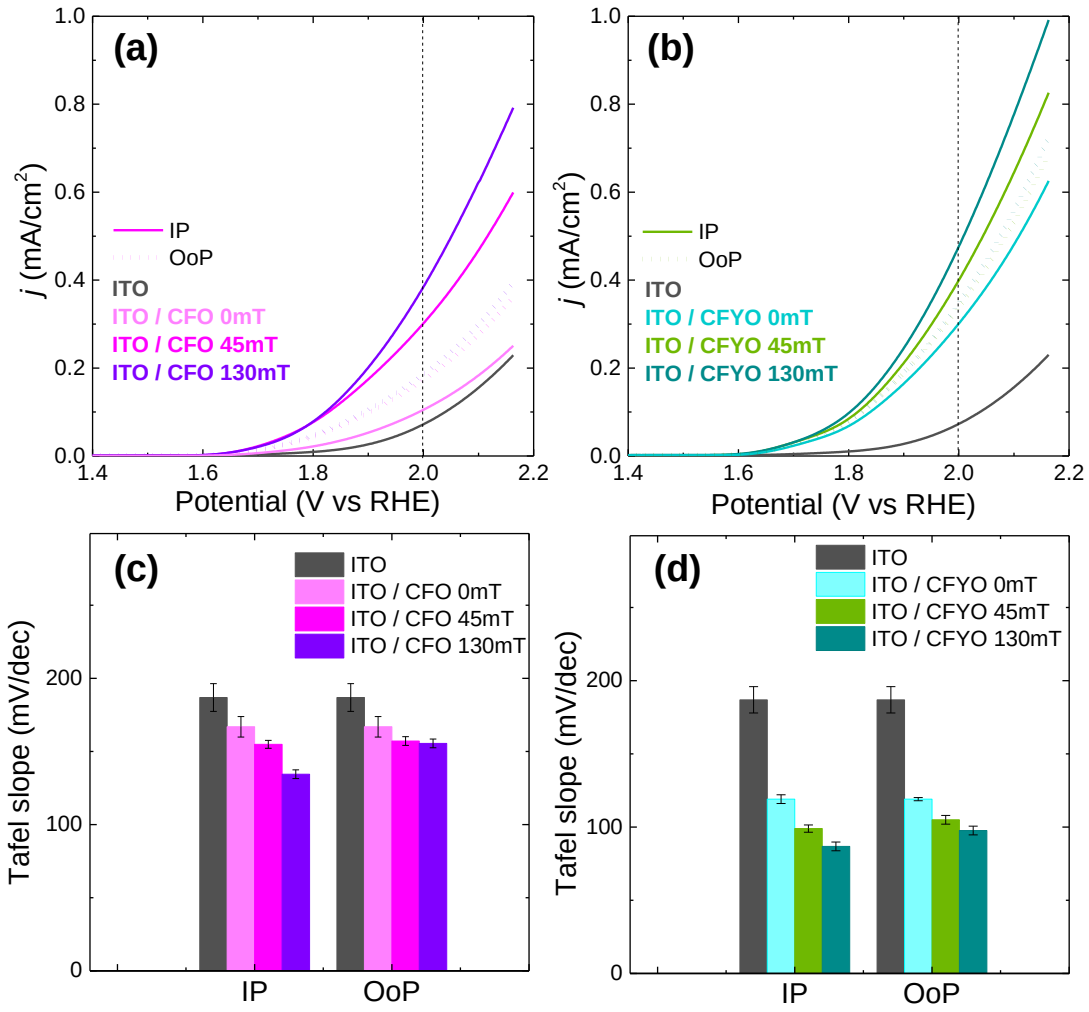

Figure 6. LSV curves of (a) ITO/CFO and (b) ITO/CFYO nanofilms in 0.1 M KOH at 25 mV·s^{-1} under zero-field (0 mT), in-plane (IP), and out-of-plane (OoP) magnetic fields at different strengths. Solid and dashed lines correspond to IP and OoP configurations, respectively. The dashed vertical line at 2.0 V indicates the potential value at which the electrode efficiencies are compared (see text). (c, d) Tafel slopes extracted from the corresponding LSV curves.

The corresponding Tafel slopes, extracted from the LSV curves, summarized in Figures 6(c) and 6(d), Figures S4, S5, and listed in Table S3 of the Supplementary Information, further support these trends. For ITO/CFO, the slope decreases from 167 mV/dec (0 mT) to 155 mV/dec at 45 mT and 134 mV/dec at 130 mT in IP, while in OoP it decreases less sharply to 158 mV/dec and 155 mV/dec for the same fields. In ITO/CFYO, the slope drops from 119 mV/dec (0 mT) to 99 mV/dec at 45 mT and 87 mV/dec at 130 mT in IP, and to 105 mV/dec and 98 mV/dec in OoP.

Overall, the lowest Tafel slopes were obtained for ITO/CFYO in the IP configuration, confirming that the combination of Y^{3+} doping and in-plane magnetic field application yields the most favorable OER kinetics among the tested conditions. It is worth noting that although the best overall OER performance is achieved when both the magnetic field and Y-doping are applied simultaneously, the ITO/CFO anode under an IP magnetic field exhibits higher current densities than the same electrode without a magnetic field and values comparable to those of the Y-doped counterpart under identical conditions. These results indicate that the magnetic field is particularly effective in enhancing the OER activity of the undoped Co ferrite electrode, offering a promising strategy to reduce or even eliminate the need for rare-earth elements. This more pronounced enhancement using pure $CoFe_2O_4$ nanofilm as anode is likely because of the higher magnetization saturation of this material.

The difference between the IP and OoP magnetic configurations can be explained by considering both magnetic anisotropy and field-induced transport effects. The anisotropic magnetic properties of the films determine the preferred direction of spin alignment, directly influencing spin-polarized charge transfer during the OER. In the case of ITO/CFO, its higher *Ms* relative to the Y^3-doped counterpart facilitates more efficient spin alignment under an external magnetic field, leading to stronger enhancement in IP configuration.[40,41] However, this improvement cannot be solely attributed to spin polarization. When the magnetic field is applied parallel to the electrode surface (IP), the current density (j) becomes orthogonal to the magnetic field (B), generating a Lorentz force ($F^L = j \times B$) that induces magnetohydrodynamic (*MHD*) convection in the electrolyte. This effect promotes ion transport, reduces diffusion limitations, and accelerates the detachment of oxygen bubbles, thereby improving mass and charge transfer at the electrode-electrolyte interface. In contrast, when the field is oriented OoP, B and j are parallel, suppressing the Lorentz force and the associated *MHD* contribution.[42-45] Therefore, the larger OER enhancement observed under IP conditions arises from the synergistic coexistence of spin-polarization-driven kinetics and Lorentz-induced *MHD* effects.

The cooperative effects of magnetic anisotropy and field-induced transport can further influence the elementary steps of the OER mechanism. In particular, the Lorentz-force-induced microconvection that arises under the IP magnetic configuration improves the accessibility of hydroxide ions and facilitates the desorption of oxygen intermediates, complementing the spin-polarization-driven electron transfer at the active sites. This synergistic interplay between spin alignment and Lorentz-induced mass transport helps to explain the lower overpotentials and Tafel slopes observed under IP magnetic fields, in accordance with recent studies on magnetic-field-assisted electrocatalysis. [42-46]

In addition to enhancing mass and charge transport, the magnetic field also affects the electronic structure of the active sites through spin polarization. The simultaneous alignment of electron spins and magnetic domains promotes spin-selective charge transfer and modifies the population of spin states involved in oxygen intermediate formation. Consequently, the catalytic surface under magnetic influence becomes more favorable for spin-allowed transitions, further accelerating the OER process. These effects are consistent with previous reports on spin-polarized OER, where an external magnetic field modifies the spin states of both catalytic sites and oxygen-containing reactants, enabling transitions that facilitate triplet O_2 formation.[41,43,47]

In alkaline media, the OER on ITO/CFO and ITO/CFYO proceeds via a four-electron pathway at surface metal sites (M) and active sites (*).[45-49] Scheme 3 (a) depicts the mechanism, which is detailed as follows:

M-OH* formation via OH^- adsorption (Step I).

$$M^* + OH^- \rightarrow M\text{-}OH^* + e^- \quad (1)$$

M-O* generation by M* + OH^- deprotonation, releasing one electron and a water molecule (Step II).

$$M\text{-}OH^* + OH^- \rightarrow M\text{-}O^* + H_2O + e^- \quad (2)$$

M-OOH* formation via nucleophilic attack of OH^- on M-O* (Step III).

$$M\text{-}O^* + OH^- \rightarrow M\text{-}OOH^* + e^- \quad (3)$$

Release of triplet-state O_2 from M-OOH* through a proton-coupled electron transfer, regenerating the active site (Step IV).

$$M\text{-}OOH^* + OH^- \rightarrow M^* + O_2 + H_2O + e^- \quad (4)$$

Overall (alkaline OER):

$$4\ OH^- \rightarrow O_2 + 2\ H_2O + 4\ e^- \quad (5)$$

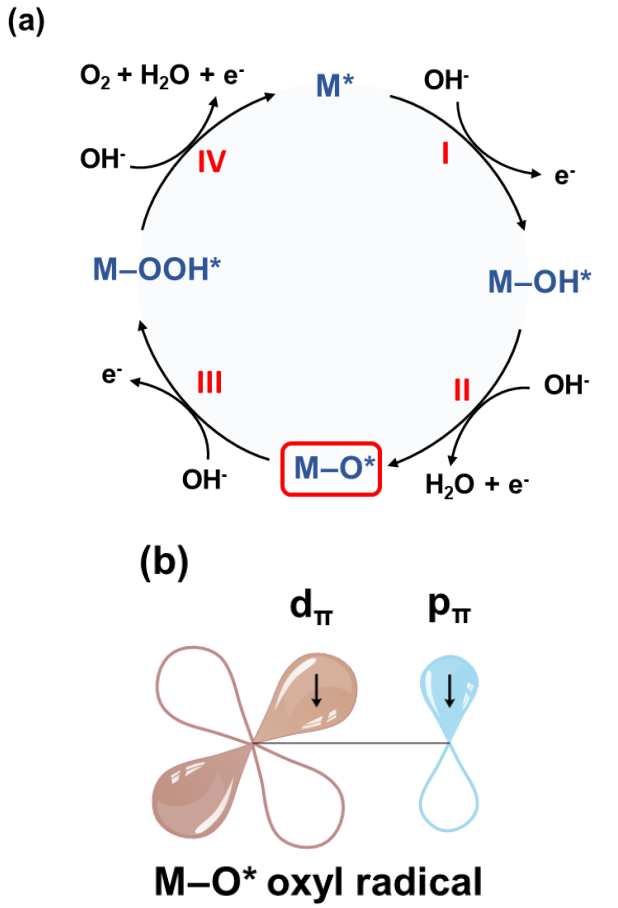

Scheme 3. (a) Spin alignment of oxyl radicals (M-O*) under an external magnetic field. (b) Spin-polarized oxygen intermediates facilitating O-O bond formation during the OER.

As mentioned before, the catalytic behavior of ferromagnetic oxides under a magnetic field can be rationalized in terms of spin polarization. In ferromagnetic catalysts, spin polarization aligns the spins of OH*, O*, and OOH* intermediates with the majority-spin states of the catalyst, facilitating spin-allowed electron transfer. [43,45] In Step II of the OER pathway, the reactive oxyl radical M-O· is generated from M-OH deprotonation, where the ligand oxygen bears unpaired electrons. As shown in Scheme 3(b), exchange interactions promote parallel spin alignment between the oxygen pπ and metal dπ orbitals, while ferromagnetic ordering polarizes neighboring ligand oxygens.[47] In cobalt ferrites, an external magnetic field further reduces spin scattering and enables coherent spin-polarized transport through the Fe-O-Co superexchange network.[40] Therefore, the enhancements observed in Figures 6(a-b) arise from the synergistic effects of Y^{3+} doping (which increases electronic conductivity) and magnetic-field-induced optimization of spin-selective charge transfer.

These effects at the electronic and transport levels are further evidenced by the electrochemical impedance spectroscopy (EIS) results discussed below. Figures 7(a)-(d) show the EIS Nyquist plots for ITO/CFO and ITO/CFYO nanofilms measured at 1.70 V vs RHE under IP and OoP magnetic fields. All measurements exhibit a semicircle in the high-to-mid frequency region, characteristic of the charge-transfer resistance (*R*ct). In both nanofilms, the application of a magnetic field leads to a clear reduction in *R*ct, indicating faster interfacial charge transfer during OER.

This effect is more pronounced in the IP configuration, in line with the higher current densities (Figures 6(a)-(b)) and lower Tafel slopes (Figures 6(c)-(d)) observed under this field orientation. In all conditions, ITO/CFYO presents smaller semicircle diameters than ITO/CFO, confirming the beneficial role of Y^{3+} doping in reducing intrinsic *R*ct and improving interfacial charge transport.

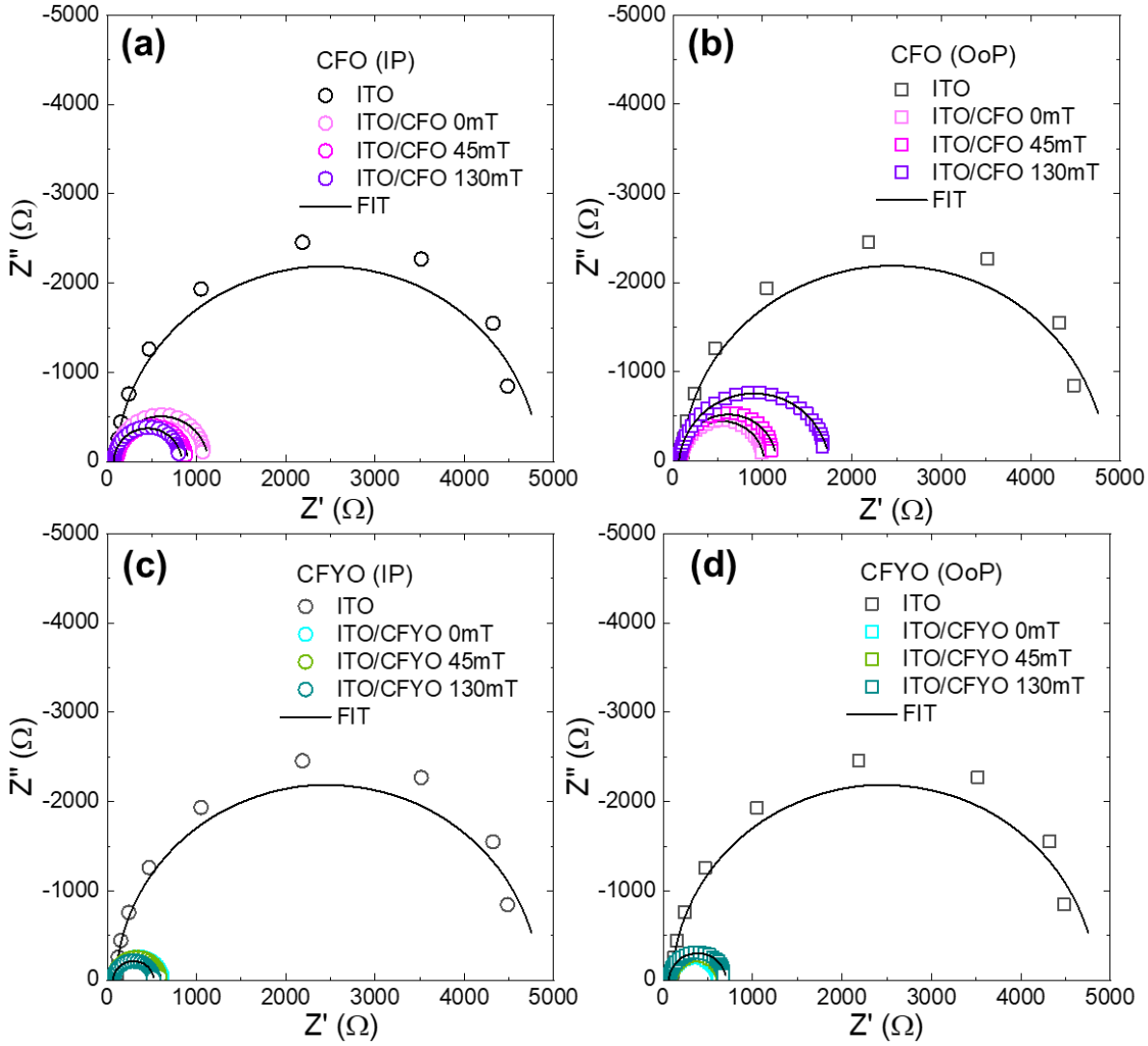

Figure 7. Nyquist plots of (a) ITO/CFO (IP), (b) ITO/CFO (OoP), (c) ITO/ ITO/CFYO (IP), and (d) ITO/CFYO (OoP) measured at 1.70 V vs RHE. Zero-field data are included for comparison. Experimental data are shown as circles (IP) and squares (OoP) and fitted using the Randles equivalent circuit (solid lines). Fitting parameters are summarized in Table S3 of the Supplementary Information

These EIS observations are fully consistent with the magnetic-field-induced enhancements in current density and reduced Tafel slopes previously shown in Figure 6, providing complementary evidence of the synergistic effects of Y^{3+} doping and magnetic anisotropy on OER performance. The EIS data were fitted with a Randles equivalent circuit, and the extracted parameters are summarized in Table S3 of the Supplementary Information. The trend *R*ct(IP) < *R*ct(OoP) holds for both materials, evidencing the anisotropic response to magnetic-field orientation. These numerical values reinforce the qualitative trends seen in Figures 7(a)-(d), showing quantitatively that both Y^{3+} doping and magnetic field application contribute to lowering *R*ct. The reduction in *R*ct under applied field is consistent with previous reports where magnetic or compositional modifications in cobalt ferrites reduced *R*ct by more than an order of magnitude, from ~2000 Ω to ~10 Ω. [39,41]

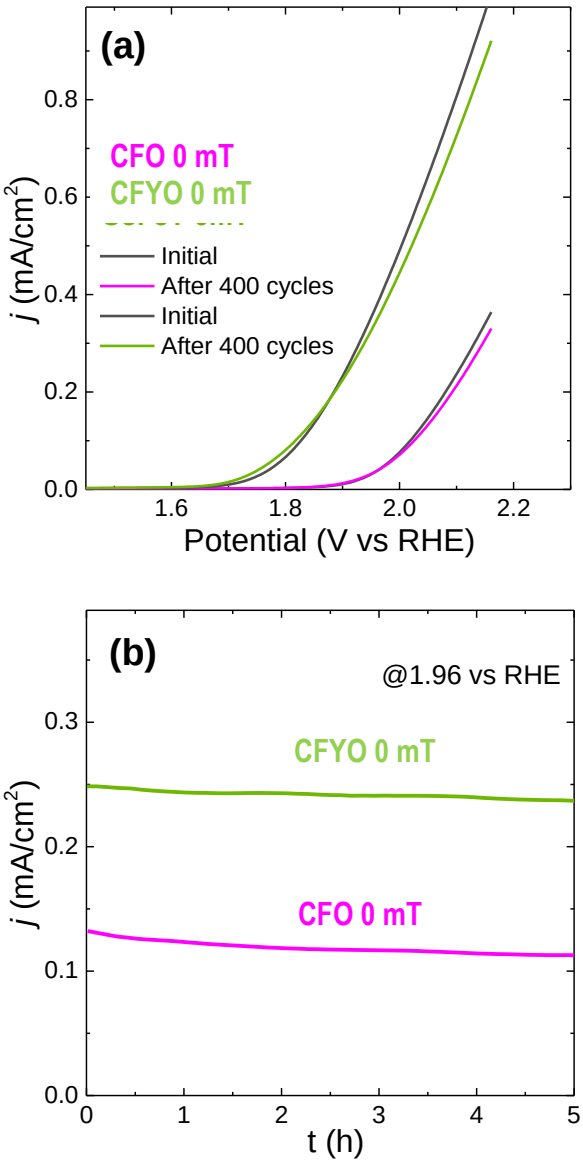

Figure 8. (a) LSV curves of ITO/CFO and ITO/CFYO films recorded before and after 400 continuous cycles at 0 mT. (b) Chronoamperometric response at 1.96 V vs. RHE for ITO/CFO and ITO/CFYO films measured for 5 h at 0 mT.

The reduction of *R*ct under magnetic field in the IP configuration reflects the synergistic action of spin polarization and Lorentz-induced magnetohydrodynamic effects. The alignment of magnetic moments and the formation of reactive oxyradical intermediates (M-O*) facilitate spin-allowed O-O bond formation, thereby lowering the kinetic barrier for the OER. Simultaneously, Lorentz-force-driven microconvection enhances ionic mobility in the electrolyte and accelerates charge exchange across the electrode-electrolyte interface, contributing to the observed decrease in interfacial resistance. In parallel, Y^{3+} incorporation increases electrical conductivity and optimizes cation distribution, further improving charge-transfer efficiency and overall catalytic performance.

The long-term stability is another important criterion to assess an electrocatalyst for electrochemical applications. The electrocatalytic stability of ITO/CFO and ITO/CFYO anodes was evaluated after 400 cycles with no applied magnetic field, as shown in Figure 8(a). The LSV obtained after 400 cycles only displays a slightly positive shift in comparison with the initial one, demonstrating that the developed anodes are efficient and stable. Additionally, chronoamperometric measurements performed at 1.96 V vs RHE for 5 h at 0 mT (Figure 8(b)) show that both electrodes maintain a nearly steady current density, with ITO/CFYO exhibiting slightly higher retention than ITO/CFO. These results further confirm the structural robustness and electrochemical durability of the films under prolonged OER operation.

Conclusion

Homogeneous $CoFe_2O_4$ and $CoY_{0.2}Fe_{1.8}O_4$ nanofilms were successfully fabricated on ITO substrates via the Langmuir-Blodgett technique, enabling precise control over film thickness and surface organization. Structural and magnetic analyses confirmed the spinel phase formation and the presence of strong in-plane magnetic anisotropy. The incorporation of yttrium ions slightly modified the crystal lattice structure and magnetic response, improved charge transfer, and enhanced electrocatalytic behavior in the OER.

Electrochemical studies demonstrated that Y^{3+} doping significantly enhances the OER activity of the nanofilms by reducing both the overpotential and the charge-transfer resistance. The application of an external magnetic field further amplifies the catalytic response, particularly under the in-plane configuration. This magnetically induced

enhancement arises from the synergistic effects of spin polarization and Lorentz-force-driven magnetohydrodynamic convection, which together facilitate more efficient charge transport and accelerate interfacial kinetics. Notably, the magneto-enhancement is even more pronounced in the undoped cobalt ferrite anodes, achieving performance levels comparable to (or exceeding) those of Y-substituted ferrites without an applied field. These findings highlight that external magnetic stimuli can effectively boost the catalytic activity of simple, low-cost materials, potentially eliminating the need for doping with scarce and expensive rare-earth elements.

Overall, the combination of Langmuir-Blodgett assembly, rare-earth doping, and the use of magnetic fields provides a promising strategy for the rational design of 2D magnetic electrocatalysts. These findings highlight the potential of magnetic spinel nanofilms as robust and efficient anodes for OER and other energy conversion applications.

Supporting Information

The Supplementary Information includes: A table summarizing binding energy and peak area values obtained from XPS spectral fitting (Table S1); magnetic parameters of the nanofilms (Table S2); AFM cross-sectional profiles (Figure S1); tables of impedance parameters extracted from equivalent-circuit fitting and Tafel slopes (Table S3); cyclic voltammetry scans recorded in a non-Faradaic region for capacitance determination (Figure S2); and cyclic voltammograms normalized by the electrochemically active surface area (ECSA) (Figure S3). Tafel slopes curves for ITO/CFO (Figure S4) and ITO/CFYO (Figure S5).

Acknowledgments

This work was partially supported by Secyt-UNC and Conicet PIP 11220200102625CO projects. Viviana Daboin acknowledges a doctoral fellowship from Conicet. We thank the 'Laboratorio de Análisis de Materiales por Espectrometría de Rayos X' (LAMARX-FAMAF-UNC; https://lamarx.famaf.unc.edu.ar/) for granting access to the scanning electron microscope.

Table of Contents Graphic

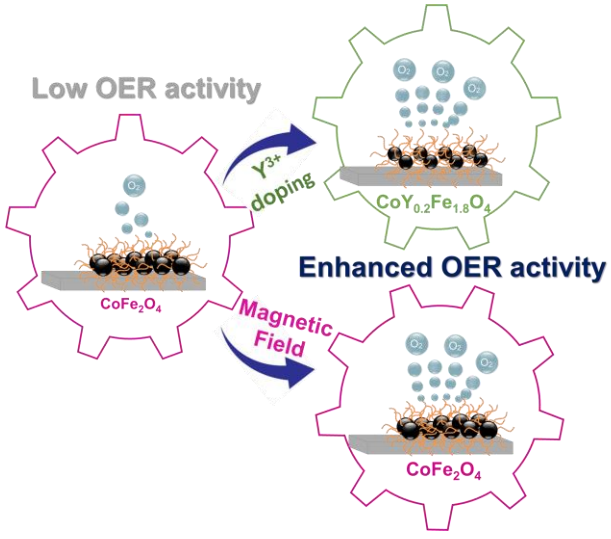

Supplementary Information

XPS characterization of the NPs

In both systems, the XPS Co 2p and Fe 2p spectra are consistent with mixed oxidation states typical of spinel ferrites, while Y^{3+} incorporation leads to subtle changes in peak positions and relative contributions, indicating modifications in the local electronic environment and cation distribution. The O 1s spectra show contributions associated with lattice oxygen and surface-related species, whereas the presence of SA coating is reflected by the increased C 1s signal and additional O 1s components related to organic functional groups. Table S1 lists the relevant parameters obtained from the fits. These results support the compositional and electronic differences discussed in the main text.

Table S1. Results of the XPS curves fitting analysis of Co ferrite and Y-substituted Co ferrite nanoparticles, after SA coating.

	CFO		**CFYO**	
Assignment	BE (eV)	Area (CPS.eV)	BE (eV)	Area (CPS.eV)
Y-O	----	----	157.59	3231.90
Y (III)	----	----	159.68	1773.23
C-C	284.75	10916.47	284.80	9138.60
C-O	286.83	232.01	285.43	6427.95
C=O	288.58	417.03	288.66	527.13
M-O	529.85	62492.54	529.50	12643.39
C-O	531.95	9578.35	531.36	6910.05
Fe (III) oct.	710.36	40468.80	710.22	7070.24
Fe (III) tetr.	712.84	20603.42	712.39	4361.60
Fe (III) sat.	717.78	41095.38	717.81	1934.38
Fe (III) sat.	731.56	12675.49	732.56	1054.32
Co (II) oct.	779.80	26006.14	779.57	5391.04
Co (II) tetr.	782.32	15396.49	781.55	3719.06
Co (II) sat.	786.42	28403.47	786.10	3687.95
Co (II) sat.	802.16	9500.21	802.13	1900.13

Characterization of ITO/CFO and ITO/CFYO nanofilms

The characteristic magnetic parameters obtained from the hysteresis loops of Figures 4(e) and 4(f) for ITO/CFO and ITO/CFYO nanofilms are summarized in Table S2. As expected, ITO/CFO nanofilm exhibits a higher saturation magnetization (M_S), while Y^{3+} incorporation leads to a reduction in M_S and a slight increase in coercivity (H_C).

Table S2. Magnetic parameters at room temperature corresponding to the nanofilms: saturation magnetization *Ms*, remanent magnetization M_R and coercive field H_C.

Sample	M_S [emu/g]	M_R [emu/g]		Hc [mT]	
		IP	OoP	IP	OoP
ITO/CFO	84 ± 3	43 ± 1	22 ± 1	123 ± 1	57 ± 1
ITO/CFYO	59 ± 3	25 ± 1	8 ± 1	150 ± 1	30 ± 1

Figure S1 shows AFM images of (a) ITO/CFO and (c) ITO/CFYO nanofilms measured in a region containing the film boundaries. **Figure S1** (b) and (d) show the corresponding cross-sectional profiles along the black dashed lines, highlighting the transition from the ITO substrate to the transferred nanofilms and allowing estimation of the film thicknesses.

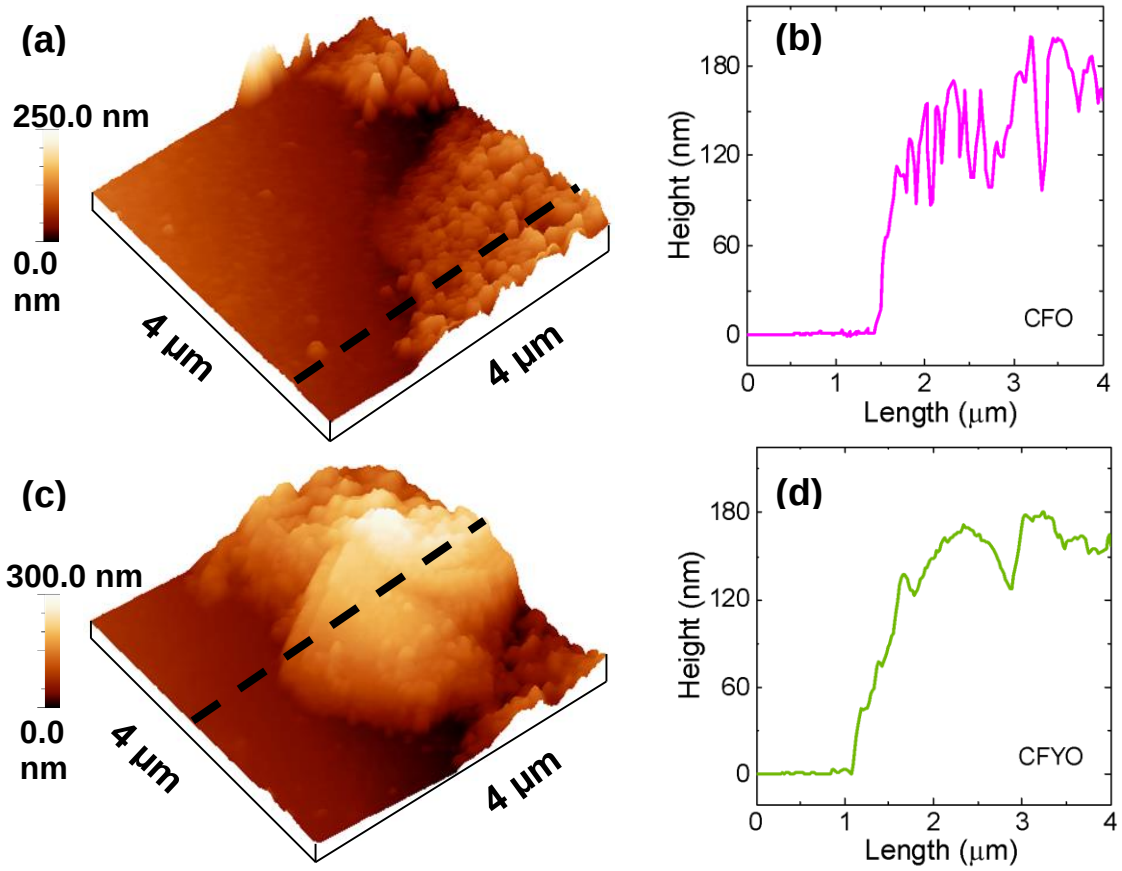

Figure S1. AFM images of (a) ITO/CFO and (c) ITO/CFYO nanofilms, and (b) and (d) the corresponding cross-sectional profiles along the black dashed lines shown in the images.

Oxygen evolution reaction performance of the nanofilms

The fitted EIS parameters for ITO/CFO and ITO/CFYO electrodes at 1.70 V vs RHE, under in-plane (IP) and out-of-plane (OoP) magnetic field configurations, are summarized in Table S3. In both nanofilms, *R*ct decreases upon applying a magnetic field, with the lowest values observed for the IP configuration at 130 mT. This reduction is particularly significant for ITO/CFYO, which exhibits smaller *R*ct values than ITO/CFO under all tested conditions, confirming the synergistic role of Y^{3+} doping in enhancing charge-transfer kinetics. The consistent trend of *R*ct(IP) < *R*ct(OoP) supports the magnetic-anisotropy-driven improvement in interfacial electron transfer.

Table S3. Electrochemical impedance parameters obtained from fitting the Nyquist plots of ITO/CFO and ITO/CFYO films. *R*s: solution resistance; *R*ct: charge-transfer resistance; CPE: constant phase element. Tafel slopes values.

Sample	Rs (Ω)	Rct (Ω)	CPE (F)	Tafel slopes (mV/dec)
ITO	98.1	4732	2.7x10-5	187
CFO 45 mT (IP)	104.2	801	2.34x10-5	155
CFO 130 mT (IP)	72.7	760	2.33x10-5	134
CFO 45 mT (OoP)	77.7	1077	2.40x10-5	159
CFO 130 mT (OoP)	65.5	1677	3.47x10-5	156
CFYO 45 mT (IP)	62.7	539	2.8x10-5	99
CFYO 130 mT (IP)	62.8	461	2.9x10-5	87
CFYO 45 mT (OoP)	71.9	603	2.7x10-5	105
CFYO 130 mT (OoP)	62.3	642	2.7x10-5	98

The catalytic activity was correlated with the electrochemical surface area (ECSA), which is linearly proportional to the electrochemical charging of the electrochemical double layer, Cdl. The Cdl was evaluated by capacitance measurement via CV in the double-layer region (0.05 to 0.15 V) with varying scan rates (Figure S2).

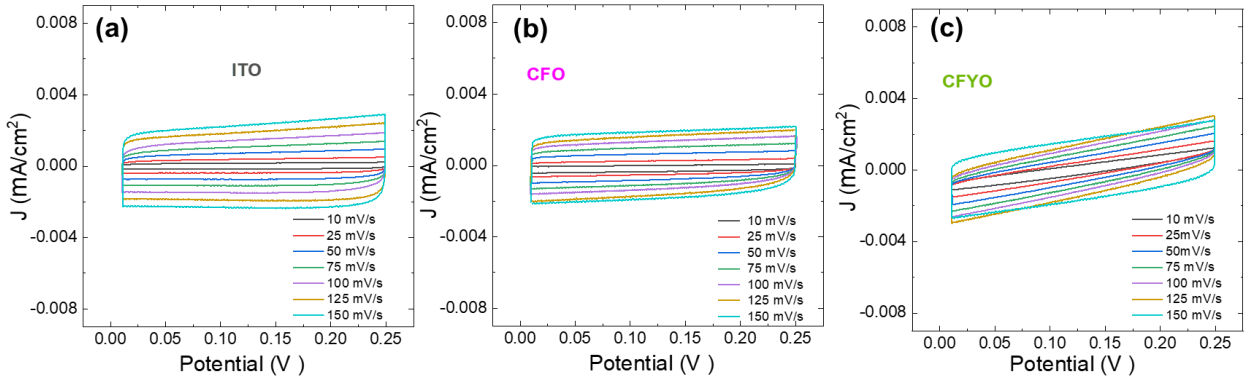

Figure S2. ECSA analysis by the CV scans in a non-Faradaic potential range of as-prepared electrodes (a) ITO, (b) CFO, (c) CFYO in 1 M KOH at scan rates of 10 mV•s^{-1}, 25 mV•s^{-1}, 50 mV•s^{-1}, 75 mV•s^{-1}, 100 mV•s^{-1},125 mV•$s^{-1}$and 150mV•s^{-1}.

Half of the differences in current density variation ($\Delta J = (J_{cathodic}-J_{anodic})/2$) plotted against the scan rate and fitted to a linear regression enables the determination of double-layer capacitance. From the Cdl values and the specific capacitance of the material (Cs) per unit area, the ECSA was calculated, and the values obtained for (a) ITO, (b) CFO, (c) CFYO were 0.1377, 0.091, and 0.1105 cm^{-2}, respectively. The LSV normalized with the ECSA area is shown in Figure S3.

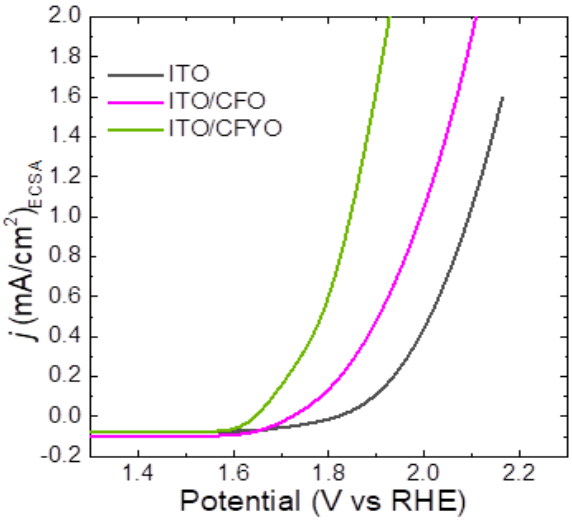

Figure S3. ECSA normalized activity of CFO and CFYO catalysts deposited on ITO.

The Tafel slopes were obtained from the LSV curves by fitting the linear region of the overpotential versus log(*j*) plots for ITO/CFO and ITO/CFYO anodes during the OER. The effects of the magnetic field intensity and the direction of its application were evaluated, as shown in Figures S4 and S5, and discussed in the manuscript.

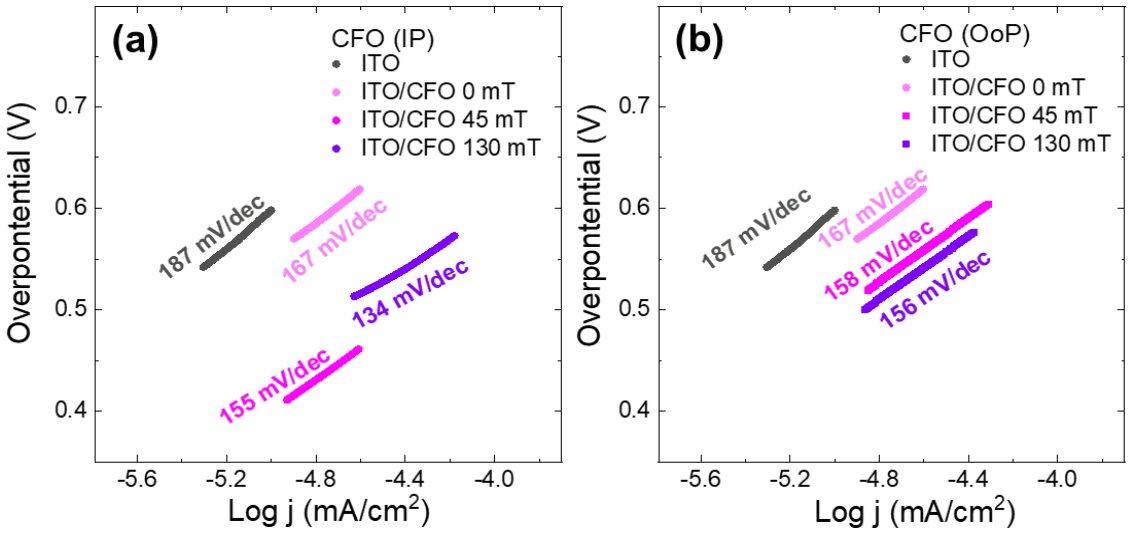

Figure S4. (a) Tafel slopes of ITO and ITO/CFO measured under zero-field (0 mT), in-plane (IP), and out-of-plane (OoP) magnetic fields of different intensities.

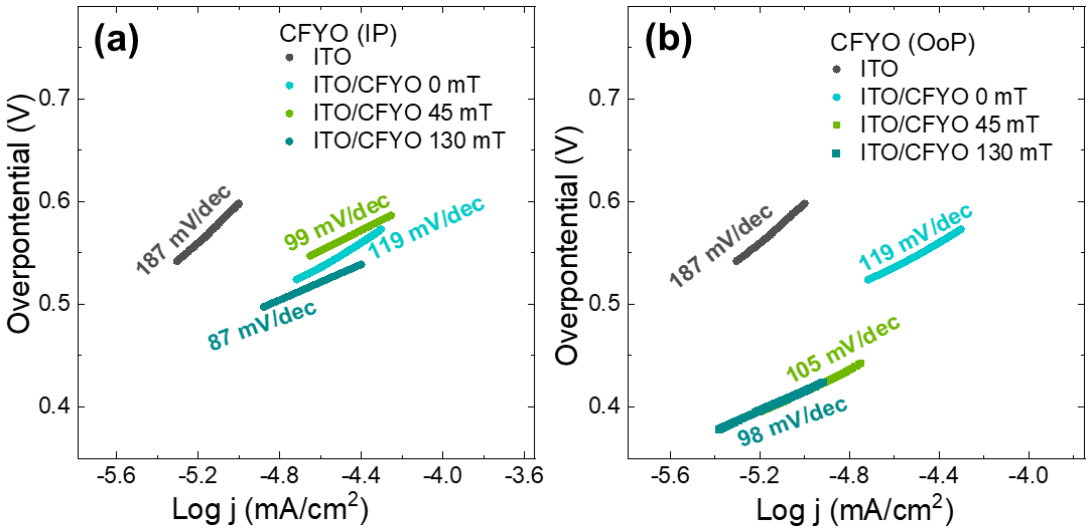

Figure S5. (a) Tafel slopes of ITO and ITO/CFYO measured in the presence and absence of an external magnetic field applied in the IP or OoP direction.

References

[1] Davis, E. M.; Bergmann, A.; Zhan, C.; Kuhlenbeck. H.; Roldan. B. Comparative study of Co_3O_4(111), $CoFe_2O_4$(111), and Fe_3O_4(111) thin film electrocatalysts for the oxygen evolution reaction. *Nat Comm.* **2023**, 14, 4791. https://doi.org/10.1038/s41467-023-40461-0.

[2] Sagu, J. S.; Mehta, D.; Upul, K. G.; Electrocatalytic activity of $CoFe_2O_4$ thin films prepared by AACVD towards the oxygen evolution reaction in alkaline media. *Electrochem. Comm.* **2018**, 87, 1-4. https://doi.org/10.1016/j.elecom.2017.12.017.

[3] Bajdich, M.; García-Mota, M.; Vojvodic, A.; Nørskov, J. K.; Bell, A. T. Theoretical investigation of the activity of cobalt oxides for the electrochemical oxidation of water. *J. Am. Chem. Soc.* **2013**, 135, 13521-13530. http://dx.doi.org/10.1021/ja405997s.

[4] Tian, J.; Li, H.; Asiri, A. M.; Al-Youbi, A. O.; Sun, X. Photoassisted preparation of cobalt phosphate/graphene oxide composites: a novel oxygen-evolving catalyst with high efficiency. *Small* **2013**, 9, 2709-2714. http://dx.doi.org/10.1002/smll.201203202.

[5] Suntivich, J.; May, K. J.; Gasteiger, H. A.; Goodenough, J. B.; Shao-Horn, Y. Perovskite oxide optimized for oxygen evolution catalysis from molecular orbital principles, *Science* **2011**, 334, 1383-1385. https://doi.org/10.1126/science.1212858.

[6] Subbaraman, R.; Tripkovic, D.; Chang, K.-C.; Strmcnik, D.; Paulikas, A. P.;Hirunsit, P.; Chan, M.; Greeley, J.; Stamenkovic, V.; Markovic, N. M. Trends in activity for the water electrolyser reactions on 3d M(Ni,Co,Fe,Mn) hydr(oxy)oxide catalysts. *Nat. Mater.* **2012**, 11, 550-557. http://dx.doi.org/10.1038/nmat3313.

[7] Zhang, C.; Bhoyate, S.; Zhao, C.; Kahol, P. K.; Kostoglou, N.; Mitterer, C.; Hinder, S. J.; Baker, M. A.; Constantinides, G.; Polychronopoulou, K.; Rebholz, C.;Gupta, R. K. Electrodeposited Nanostructured $CoFe_2O_4$ for Overall Water Splitting and Supercapacitor

Applications. *Catalysts*, **2019**, 9(2), 176. https://doi.org/10.3390/catal9020176

[8] Afaq, M. Shahid, M.; Ahmad, I.; Yousaf, S.; Alazmi, A.; Mahmoud, M. H. H.; El Azabf, I. H.; Warsi, M. F. Large-scale sonochemical fabrication of a Co_3O_4-$CoFe_2O_4$@MWCNT bifunctional electrocatalyst for enhanced OER/HER performances. *RSC Adv.* **2023**, 13, 19046-19057. https://doi.org/10.1039/D3RA03117A.

[9] Yeh, C. H.; Hsu,W. Y.; Hsu, C. C.; Valinton, J. A. A.; Yang, C. I.; Chiu, C. C.; Chen, C. H. Cobalt-Iron Oxides Prepared by Acidic Redox-Assisted Precipitation: Characterization, Applications, and New Opportunities. *ACS Appl. Mater. Interfaces* **2021**, 13, 52181-52192. https://doi.org/10.1021/acsami.1c11217

[10] Dunn, I. H.; Jacobo, S. E.; Bercoff, P. G. Structural and magnetic influence of yttrium-for-iron substitution in cobalt ferrite. *J. All. Comp.* **2021** 691, 130-137. http://dx.doi.org/10.1016/j.jallcom.2016.08.223.

[11] Daboin, V. B.; Riva, J. S.; Bercoff, P. G. Magnetic nanofilms prepared by Langmuir-Blodgett nanoarchitectonics using Co and Co-Y ferrite nanoparticles. *Mater. Res. Bull.* **2025**, 189, 113449. https://doi.org/10.1016/j.materresbull.2025.113449.

[12] Karakas, İ. H. The effects of fuel type onto the structural, morphological, magnetic and photocatalytic properties of nanoparticles in the synthesis of cobalt ferrite nanoparticles with microwave assisted combustion method. *Ceram. Int*. **2021**, 47, 5597-5609. https://doi.org/10.1016/j.ceramint.2020.10.144.

[13] Yan, C. H.; Xu, Z. G.; Cheng, F. X.; Wang, Z. M.; Sun, L. D.; Liao, C. S.; Jia, J. T. Nanophased $CoFe_2O_4$ prepared by combustion method, *Solid State Comm.* **1999**, 111, 287-291. https://doi.org/10.1016/S0038-1098(99)00119-2.

[14] Al Maashani, M. S.; Khalaf, K. A.; Gismelseed, A. M.; Al-Omari, I. A. The structural and magnetic properties of the nano-$CoFe_2O_4$ ferrite prepared by sol-gel auto-combustion technique. *J. All. Comp.* **2020**, 817, 152786. https://doi.org/10.1016/j.jallcom.2019.152786.

[15] Bera, P.; Lakshmi, R. V.; Prakash, B. H.; Tiwari, K.; Shukla, A.; Kundu, A. K.; Biswas, K.; Barshilia, H. C. Solution combustion synthesis, characterization, magnetic, and dielectric properties of $CoFe_2O_4$ and $Co_{0.5}M_{0.5}Fe_2O_4$ (M = Mn, Ni, and Zn). *Phys. Chem. Chem. Phys*. **2020**, 22, 20087-20106. https://doi.org/10.1039/d0cp03161e.

[16] Rajan Babu, D.; Venkatesan, K. Synthesis of nanophasic $CoFe_2O_4$ powder by self-igniting solution combustion method using mix up fuels. *J. Cryst. Growth* **2017**, 468 179-184. https://doi.org/10.1016/j.jcrysgro.2016.11.054.

[17] Daboin, V. B.; Riva, J. S.; Bercoff, P .G.; Magnetic behavior of nanofilms prepared by assembling different Co ferrite nanoparticles, *Mater. Res. Bull.* **2025,** 184, 113229. https://doi.org/10.1016/j.materresbull.2024.113229.

[18] Ullah S.; Shabir M.; Rasheed M.A.; Ahmad I.; Ahmed E.; Ahmad M.; Khalid N.R.; Khan W.Q. Silver and yttrium co-doped ZnO nanoparticles as a potential water splitting photocatalyst for the H_2 evolution reaction. *J Sol-Gel Sci Technol* 2023, 108, 756–767 (). https://doi.org/10.1007/s10971-023-06222-7.

[19] He D.; Gao R.; Liu S.; Sun M.; Liu X.; Hu K.; Su Y.; Wang L.; Yttrium-Induced Regulation of Electron Density in NiFe Layered Double Hydroxides Yields Stable Solar Water Splitting, *ACS Catal.* **2020**, 10, 10570−10576. https://dx.doi.org/10.1021/acscatal.0c03272

[20] Li, Y.; Zhang, L.; Peng, J.; Zhang, W.; Peng, K. Magnetic field enhancing electrocatalysis of Co_3O_4/NF for oxygen evolution reaction, *J. Power Sources* **2019**, 433, 226704. https://doi.org/10.1016/j.jpowsour.2019.226704.

[21] Garcés-Pineda, F. A.; Blasco-Ahicart, M.; Nieto-Castro, D.; López, N.; Galán-Mascarós, J. R. Direct magnetic enhancement of electrocatalytic water oxidation in alkaline

media. *Nature Energy* **2019**, 4, 519-525. https://doi.org/10.1038/s41560-019-0404-4

[22] Zheng, H.; Wang, Y.; Zhang, P.; Ma, F.; Gao, P.; Guo, W.; Qin, H.; Liu, X.; Xiao, H. *Chem. Eng. J.* **2021**, 426, 130785. https://doi.org/10.1016/j.cej.2021.130785.

[23] Huang, Q.; Xie, S.; Hao, J.; Ding, J.; Zhang, C.; Sheng, H.; Zhaom, J. Spin-Enhanced O−H Cleavage in Electrochemical Water Oxidation. *Angew. Chem. Int. Ed.* **2023**, 62, e202300469. https://doi.org/10.1002/anie.202300469

[24] Sun, Y.; Lv, H.; Yao, H.; Gao, Y.; Zhang, C. Magnetic field-assisted electrocatalysis: Mechanisms and design strategies. *Carbon Energy* **2024**, 6(10), e575. https://doi.org/10.1002/cey2.575.

[25] Kaliyaraj, A.; Kumar, S.; Zhang, Y.; Li, D.; Compton, R. G. A mini-review: How reliable is the drop casting technique?. *Electrochem. Comm.* **2020**, 121, 106867. https://doi.org/10.1016/j.elecom.2020.106867.

[26] Daboin, V. B.; Moya Betancourt, S. N.; Farias E. D.; Riva, J. S.; Bercoff, P .G. Enhancement of the electrochemical oxygen evolution reaction by light and external magnetic fields, using hybrid electrodes made by Langmuir–Blodgett. *Electrochim. Acta* **2024**, 480, 143910.

[27] Thampi, A.; Babu, K.; Verma, S. Large scale solvothermal synthesis and a strategy to obtain stable Langmuir-Blodgett film of $CoFe_2O_4$ nanoparticles. *J. All. Comp.* **2013**, 564, 143-150. https://doi.org/10.1016/j.jallcom.2013.02.139

[28] Liu, C.; Shan Y.; Zhu, Y.; Chen, K. Magnetic monolayer film of oleic acid-stabilized Fe_3O_4 particles fabricated via Langmuir-Blodgett technique, *Thin Solid Films* **2009**, 518, 324-327. https://doi.org/10.1016/j.tsf.2009.07.052.

[29] Machida, H.; Kikuchib, N.; Ohashia, T.; Fujimori, A. Analysis of soft and hard nanoparticle alternating multilayers for the development of theory for long-period stacking order structure prepared by Langmuir-Blodgett method. *Thin Solid Films* **2020**, 709, 138235. https://doi.org/10.1016/j.tsf.2020.138235.

[30] Patil, S.; Meti, S.; Kanavi, P. S.; Bhajantri, R. F.; Anandalli, M.; Mondal, R.; Karmakar, S.; Muhiuddin, M.; Rahman, M. R.; Kumar, B. C.; Hegde. B. G. A study on solubility of bismuth cations in nickel cobalt ferrite nanoparticles and their influence on dielectric and magnetic properties. *Mater. Sci. Eng. B* **2023**, 296 (11) 116570. https://doi.org/10.1016/j.mseb.2023.116570.

[31] Kumar, Y.; Sharma, A.; Ahmed, M. A.; Mali, S. S.; Hong, C. K.; Shirage. P. M. Morphology-controlled synthesis and enhanced energy product (BH) max of $CoFe_2O_4$. *New J. Chem.* **2018**, 42(19), 15793-15802. https://doi.org/10.1039/C8NJ02177E.

[32] Meng, X.; H. Li.; J. Chen, Mei, L.; Wang, K.; X. Li, Mössbauer study of cobalt ferrite nanocrystals substituted with rare-earth Y^{3+} ions. *J. Magn. Magn. Mater.* **2009**, 321, 1155-1158. https://doi.org/10.1016/j.jmmm.2008.10.041.

[33] Kumari, S.; Kumar, V.; Kumar, P.; Kar, M.; Kumar, L. Structural and magnetic properties of nanocrystalline yttrium substituted cobalt ferrite synthesized by the citrate precursor technique. *Adv. Powder Technol.* **2015**, 26, 213e223. https://doi.org/10.1016/j.apt.2014.10.002.

[34] Rajaji, U.; Chinnapaiyan, S.; Chen, S. M.; Govindasamy, M.; Oliveira Filho, J. I.; Khushaim, W.; Mani, V. Design and Fabrication of Yttrium Ferrite Garnet-Embedded Graphitic Carbon Nitride: A Sensitive Electrocatalyst for Smartphone-Enabled Point-of-Care Pesticide (Mesotrione) Analysis in Food Samples. *ACS Appl. Mate. & Interfaces* **2021**, 13, 24865-24876. doi: 10.1021/acsami.1c04597.

[35] Eskandari, F.; Porter, S. B.; Venkatesan, M.; Kameli, P.; Rode, K.; Coey, J. M. D. Magnetization and anisotropy of cobalt ferrite thin films, *Phys. Rev. Mater* **2017**, 1, 074413. https://doi.org/10.1103/PhysRevMaterials.1.074413.

[36] Ahmada, T.; Lonea, I. H.; Ansarib, S.G; Ahmedc, J.; Ahamadc, T.; Alshehric, S. M. Multifunctional properties and applications of

yttrium ferrite nanoparticles prepared by citrate precursor route. *Mater. Des.* **2017**, 126, 331-338. https://doi.org/10.1016/j.matdes.2017.04.034

[37] Ullah, S.; Shabir, M.; Rasheed, M. A.; Ahmad, I.; Ahmed, E.; Ahmad, M.; Khalid, N. R.; Khan, W. Q. Silver and yttrium co-doped ZnO nanoparticles as a potential water splitting photocatalyst for the H_2 evolution reaction. *J. Sol-Gel Sci. Technol.* **2023**, 108, 756-767. https://doi.org/10.1007/s10971-023-06222-7

[38] Li, M.; Xiong, Y.; Liu, X.; Bo, X.; Y. Zhang, Han, C.; Guo. L. Facile synthesis of electrospun MFe_2O_4 (M = Co, Ni, Cu, Mn) spinel nanofibers with excellent electrocatalytic properties for oxygen evolution and hydrogen peroxide reduction. *Nanoscale* **2015**, 7, 8920-30. doi: 10.1039/c4nr07243j.

[39] Saddeler, S.; Bendt, G.; Salamon, S.; Haase, F. T.; Landers, J.; Timoshenko, J.; Rettenmaier, C.; Jeon, H. S.; Bergmann, A.; Wende, H.; Roldan Cuenya, B.; Schulz. S. Influence of the cobalt content in cobalt iron oxides on the electrocatalytic OER activity. *J. Mater. Chem. A* **2021**, 9, 25381-25390. https://doi.org/10.1039/D1TA06568H.

[40] Ge, J.; Ren, X.; Chen, R. R.; Sun, Y.; Wu, T.; Hoong Ong, S. J.; Xu, Z. J. Multi-Domain versus Single-Domain: A Magnetic Field is Not a Must for Promoting Spin-Polarized Water Oxidation. *Angew. Chem. Int. Ed.* **2023**, 62, e202301721. https://doi.org/10.1002/anie.202301721.

[41] Singh, S.; Khare. N. Low field magneto-tunable photocurrent in $CoFe_2O_4$ nanostructure films for enhanced photoelectrochemical properties. *Sci. Rep.* **2018**, 8 6522. https://doi.org/10.1038/s41598-018-24947-2

[42] Sun, Y.; Lv, H.; Yao, H.; Gao, Y.; Zhang. C. Magnetic field-assisted electrocatalysis: Mechanismsand design strategies. *Carbon Energy* **2024**, 6, https://doi.org/10.1002/cey2.575.

[43] Feng, Z.; Dai, C.; Wang, H.; Guo, R.; You, J.; Liu, X. Recent development of external magnetic field assisted oxygen evolution reaction - A mini review. *ChemCatChem* **2023**, 15, e202300688. https://doi.org/10.1002/cctc.202300688.

[44] Su, P.; Shang, L.; Luo, L.; Li, R.; Jiang, H.; Zhou, S.; Chen, Y.; Zhu, J.; Sun, Z.; Zhang, J.; Liao, B.; Lin, L. Enhancement of Oxygen Evolution Electrocatalysis via Magnetohydrodynamic Effect on Mass Transport. *ACS Appl. Mater. Interfaces* **2025**, 17, 44, 60502–60508. https://pubs.acs.org/doi/10.1021/acsami.5c13744 .

[45] Ren, X.; Wu, T.; Sun, Y.; Li, Y.; Xian, G.; Liu, X.; Shen, C.; Gracia, J.; Gao, H. J.; Yang, H.; Xu, Z. J. Spin-polarized oxygen evolution reaction under magnetic field. *Nature Comm.* **2021**, 12, 2608. https://doi.org/10.1038/s41467-021-22865-y.

[46] Wang, K.; Yang, Q.; Zhang, H.; Zhang, M.; Jiang, H.; Zheng, C.; Li, J. Recent advances in catalyst design and activity enhancement induced by a magnetic field for electrocatalysis, *J. Mater. Chem. A* **2023**, 11, 7802-7832. https://doi.org/10.1039/D2TA09276J.

[47] Li, J. Oxygen Evolution Reaction in Energy Conversion and Storage: Design Strategies Under and Beyond the Energy Scaling Relationship. *Nano-Micro Letters* **2022**, 14**.** https://doi.org/10.1007/s40820-022-00857-x.

[48] Wu, T.; Ren, X.; Sun, Y.; Sun, S.; Xian, G.; Scherer, G. G.; Fisher, A. C.; Mandler, D.; Ager, J. W.; Grimaud, A.; Wang, J.; Shen, C.; Yang, H.; Gracia, J.; Gao, H. J.; Xu, Z. J. Spin pinning effect to reconstructed oxyhydroxide layer on ferromagnetic oxides for enhanced water oxidation. *Nature Comm*. **2021**, 12. https://doi.org/10.1038/s41467-021-23896-1.

[49] Wu, T.; Xu, Z. J. Oxygen Evolution in Spin-sensitive Pathways. *Curr. Opin. Electrochem.* **2021**, 30 100804. https://doi.org/10.1016/j.coelec.2021.100804Get rights and content